# Development and Testing of a Miniaturized, Dual-Frequency, Software-Defined GPS Receiver for Space Applications

APPROVED BY

SUPERVISING COMMITTEE:

_____

E. Glenn Lightsey, Supervisor

_____

Todd Humphreys

# Development and Testing of a Miniaturized, Dual-Frequency, Software-Defined GPS Receiver for Space Applications

by

## Andrew Jonathan Joplin, B.S.As.E.

**THESIS**

Presented to the Faculty of the Graduate School of

The University of Texas at Austin

in Partial Fulfillment

of the Requirements

for the Degree of

**MASTER OF SCIENCE IN ENGINEERING**

THE UNIVERSITY OF TEXAS AT AUSTIN

December 2011

Dedicated to the one and only love of my life and fiancée, Kyrie Callahan, and to our LORD who brought us together. I love you with all of my heart, and thank God daily for your love and support.

# Acknowledgments

# Development and Testing of a Miniaturized, Dual-Frequency, Software-Defined GPS Receiver for Space Applications

Andrew Jonathan Joplin, M.S.E.
The University of Texas at Austin, 2011

Supervisor: E. Glenn Lightsey

While dual-frequency GPS receivers have been used in space for more than two decades, the size, power, and cost of this technology is an important driver for future space missions. The growing availability of launch opportunities for very small satellites known as nanosatellites and CubeSats raises the possibility of more affordable access to space measurements if the observation quality is sufficient to support the user's needs.

This thesis presents the initial development and testing of the Fast, Orbital, TEC, Observables, and Navigation (FOTON) receiver: a small, reconfigurable, dual-frequency, space-based GPS receiver. Originally developed as a science-grade software receiver for monitoring ionospheric scintillation and total electron content (TEC), this receiver was designed to provide high-quality GPS signal observations. The original receiver hardware was miniaturized and the software has been adapted for low earth orbit (LEO) operations. FOTON now fits within a 0.5U CubeSat form factor (8.3 x 9.6 x 3.8 cm), weighs 326 g, and consumes 4.5 W of instantaneous power, which can be reduced to <1 W

orbit average power with on-off duty cycling. The receiver has been designed with commercial parts to keep manufacturing costs low.

Significant testing of FOTON has been performed with live signals and with signals generated by a Spirent GPS signal simulator. Initial terrestrial tests demonstrate behavioral consistency with the original heritage high-performance receiver. Several LEO simulations are presented, demonstrating FOTON's single-frequency and dual-frequency-enhanced positioning down to 0.5 m and 1.5 m, respectively, which can be improved using Kalman filter based POD. FOTON's potential for GPS radio occultation observation is also demonstrated. In addition, its acquisition and reacquisition performance is presented; on average, FOTON's time to first fix is approximately 45 seconds. Finally, navigation in geostationary orbit (GEO), a challenging application for space-based GPS receivers, is demonstrated. Extensive testing demonstrates that FOTON is a robust, versatile, high-precision dual-frequency space receiver. Its low cost, size, weight, and power requirements are key enablers for future small-satellite missions.

# Table of Contents

# List of Tables

# List of Figures

# Chapter 1

# Introduction

The advent of the Global Positioning System (GPS) has revolutionized many technical fields, from terrestrial navigation, for which it was originally designed, to space science research. GPS is also used as a consistent, accurate timing reference in many applications, such as telecommunication, the financial sector, and large office complexes. This study, however, focuses on the navigation and scientific applications of space-based GPS receivers, with special attention given to small satellite applications.

GPS satellites can transmit on three frequencies, known as L1, L2, and L5. The signals use code-division multiple access (CDMA) to avoid cross-satellite interference, and to allow multiple signals to be transmitted from each satellite on each frequency. Because GPS was developed and maintained by the United States military, some of the signals transmitted by the satellites are encrypted. However, all GPS satellites transmit a public-use coarse acquisition (C/A) signal on the L1 frequency. In addition to L1 C/A, some of the newer satellites transmit an additional unencrypted signal on the L2 frequency (L2C). Because the L1 C/A signal is sufficient for most civilian applications, such as in-car navigation systems and most timing applications, the vast majority of civilian GPS receivers only track this signal. However, the additional L2C signal can be used by high-precision receivers to directly eliminate the effects of the ionosphere, a large source of measurement error.

The position, velocity, and timing (PVT) requirements for satellites varies according to the mission. Some satellites, such as some of the student-built CubeSats developed by the University of Texas at Austin (UT-Austin) Satellite Design Laboratory, require only very coarse navigation capability. Major space science missions, however, often require precise (sub-meter) navigation. One example is the Gravity Recovery and Climate Experiment (GRACE), which uses K-band range measurements to detect changes in Earth's local gravitational field [7]. This requires high-precision knowledge of the GRACE satellites' positions. Some small satellite missions (such as FASTRAC [5]) involve relative navigation of two satellites, and could lead to automated rendezvous and docking demonstrations. The higher precision required for such goals can be attained using dual-frequency GPS receivers.

Another use for dual-frequency receivers on satellites is ionospheric research. A typical ionospheric research mission, such as the Constellation Observing System for Meteorology, Ionosphere, and Climate (COSMIC) mission [3], involves relatively large, expensive satellites. If such a mission could be accomplished using CubeSats, the science return per dollar spent would be significantly higher. However, current space-qualified receivers that provide such precision are too large and have too high power requirements to be practical on small satellites (see left-hand side of Figure 1.1). A small, low-power, dual-frequency GPS receiver would make such space science missions achievable.

This work presents a small, dual-frequency receiver that is under development, and is expected to be the primary navigation sensor on UT's upcoming ARMADILLO mission. The Fast, Orbital, TEC[1], Observables, and Naviga-

_____

[1]Total Electron Content

2
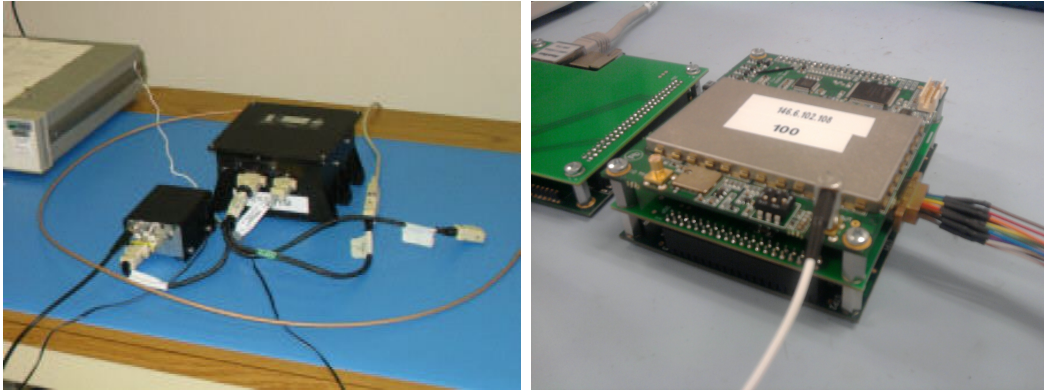
Figure 1.1: BlackJack (left) and FOTON (right) Dual Frequency Receivers

tion (FOTON) receiver is a miniaturized version of a dual-frequency terrestrial science receiver developed by Cornell University and The University of Texas at Austin. As part of this research, changes have been made to FOTON's software to allow it to navigate in the more challenging environment of space. Some additions have also been made to the software to improve its performance, including an orbital Kalman filter to supplement the existing point solution algorithm. The results of considerable testing are also presented to demonstrate FOTON's capabilities in a variety of scenarios, including both static and simple dynamic terrestrial tests, single- and dual-frequency low Earth orbit (LEO) tests, and a geosynchronous orbit (GEO) test.

The next chapter presents a brief overview of software receivers in general, and FOTON specifically. It also summarizes the major changes that needed to be made in order for FOTON to navigate on orbit, most of which were either discovered or verified by the testing presented in Chapter 3. In addition to describing the setup and procedures used in testing FOTON, Chapter 3 presents the results of the initial characterization of the CASES and FOTON receivers, comprising a live-sky test, static and dynamic terrestrial simulations,

and two LEO simulations. Chapter 4 examines FOTON's signal acquisition and reacquisition performance as a precursor to an in-depth duty cycling study. This is followed in Chapter 5 by a description of a LEO extended Kalman filter designed by the author. This filter provides a core capability that can be later improved to make possible sub-meter precision orbit determination. Chapter 6 presents the results of the initial dual-frequency LEO simulation testing; it compares several single- and dual-frequency configurations to illustrate FOTON's dual-frequency navigation performance. This is followed by a brief overview of radio occultation and an example of how FOTON can be used to measure entire local ionospheric delay profiles. Finally, Chapter 8 demonstrates FOTON's navigation capability in a geosynchronous orbit simulation, an accomplishment made possible through the use of a high-precision timing reference and the reconfigurability of a software receiver.

# Chapter 2

# Background

FOTON is a dual-frequency, software-defined GPS receiver adapted from the Connected Autonomous Space Environment Sensor (CASES) receiver developed by Cornell University and The University of Texas at Austin. The CASES receiver consists of a radio frequency (RF) front end, a single-board computer (SBC), and a digital signal processor (DSP) chip. The software that runs on CASES is the GNSS Receiver Implementation on a DSP (GRID) code, written in C++. FOTON, the space-based version of the receiver, uses the same hardware as CASES, repackaged to fit within a 0.5U CubeSat volume (approximately 8.3×9.6×3.8 cm). FOTON runs an altered version of the GRID code that was developed in this research and works in low earth orbit. This section discusses the advantages of software receivers in general, and provides a brief overview of the original GRID code, the CASES receiver, and FOTON. A summary of the changes required to make FOTON function in LEO is also provided.

## 2.1   Software Receivers

Traditional GPS receivers are composed of general-purpose processors and application-specific integrated circuits (ASICs). The signal correlation is performed on ASICs, while tracking and navigation are performed on the processor. This is acceptable in most cases, because there is often no reason to

make changes to the receiver. Software-defined receivers, however, ingest raw digital signals from a data acquisition (DAQ) board and perform correlation as well as tracking and navigation on a general-purpose processor.

Software-defined receivers have recently been gaining popularity due to the ease with which any part of the receiver, from navigation all the way down to correlation, can be changed. This allows for significantly decreased development time, as well as greater receiver customization. When considering space-based GPS receivers, this advantage becomes even more pronounced; if a bug is found in the receiver when it is already on-orbit, or if additional functionality is desired, the same satellite may still be used by simply uploading new software to the receiver. As will be demonstrated in Chapter 8, the ability to make changes to a receiver's correlation opens up the possibility of using a single receiver design for geosynchronous orbit positioning in addition to terrestrial and low Earth orbit positioning. While it is true that software receivers, in general, have higher power requirements than their hardware-based counterparts, the recent advancements in microprocessor technology renders this disadvantage insignificant compared with the flexibility offered by software receivers.

## 2.2   GRID Code

The GRID code processes a stream of binary, intermediate frequency (IF) sign, magnitude, and clock data from an RF front end, tracking GPS L1 C/A and L2C signals, and producing a navigation solution (see Fig. 2.1). The data can be input to a DSP in real-time from the front end, or it can be recorded and used as input to the equivalent post-processing receiver (PpRx). PpRx is a post-processing implementation of GRID, designed to be compiled

6
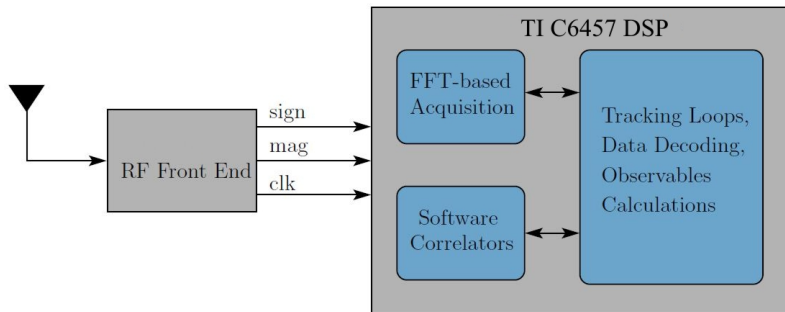
Figure 2.1: Schematic Representation of GRID [10]

and run on any Linux computer. It shares most of the same code as the real-time, DSP-based receiver, so the only difference in behavior should be run-time speed.

The GRID code is designed to take advantage of the object-oriented programming capabilities of C++. Signal tracking is handled by two main classes: `Bank` and `Channel` (Fig. 2.2). The `Bank` class contains all of the information required for tracking a specific signal type; it is inherited by such classes as `BankGPSL1CA` and `BankGPSL2C`. Although GRID is capable of tracking other signal formats, such as L5 and other CDMA signals, this report will focus on L1 C/A and L2C only.

Each bank has an array of channels that track specific signals (from individual GPS satellites, for instance). The `Channel` class has pointers to its various loops (PLL, FLL, DLL) and its observables, all of which are also contained within classes. Each channel is responsible for tracking its one specific signal and computing its observables.

Finally, the `NavSol` class uses the observables from the L1 C/A channels to compute a navigation solution, consisting of receiver position, velocity, and time, as well as receiver clock bias and rate. While in dual-frequency mode,
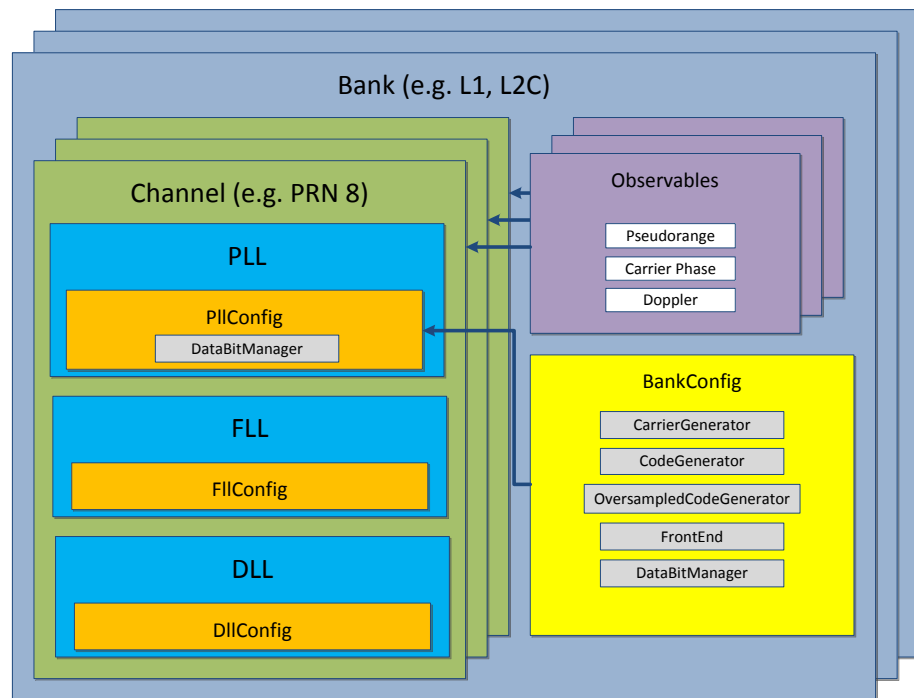
Figure 2.2: GRID Class Diagram

L2C observables are used to compute ionospheric delay. There are, of course, many other classes that perform various tasks from correlation to unpacking the broadcast navigation messages; for brevity, however, these classes are not discussed in detail.

## 2.3   CASES Receiver

The CASES receiver is constructed from commercial, off-the-shelf (COTS) components on custom-built circuit boards (Fig. 2.3). It consists of four boards:

- RF Front End

- Digital Signal Processor (DSP)

- Single-Board Computer (SBC)

- Interface Board

The RF front end, developed by Dan Bobyn Engineering, Ltd., down-converts L1 and L2 signals to an intermediate frequency of 298.73 MHz, samples at 5.714286 MHz, and quantizes the digital signal using two-bit quantization (sign and magnitude) [2]. It accepts a single antenna input, as well as an optional external clock reference input. In the absence an external clock reference, the front end uses an internal Temperature-Controlled Crystal Oscillator (TCXO).

The quantized digital signal is then fed into a reprogramable, 1 GHz Texas Instruments C6457 DSP board for processing [13]. The DSP, using the GRID code described in the previous section, is responsible for acquiring and

Figure 2.3: CASES Receiver in Two Form Factors [14]

tracking GPS L1 and L2 signals, computing pseudorange, Doppler, and carrier phase observables, and computing a navigation solution from the observables. The DSP is the heart of the receiver.

The processed channel data, along with the navigation solution, are then output in a binary format to the single-board computer (SBC). The SBC acts as an interface between the user and the DSP. Channel and navigation solution data can be retrieved, and commands issued, from a client computer remotely connected to the SBC (through the internet, for instance).

Because the front end and DSP operate on different voltages, and are both controlled by the SBC, a custom-made interface board is used to allow communication between the front end, DSP, and SBC. The interface board also has a serial port for direct user communication with the DSP (bypassing the SBC).

## 2.4   FOTON Receiver

FOTON (Fig. 2.4) is a miniaturized version of the CASES receiver. It has mostly the same hardware as CASES, but reconfigured into a smaller form factor (8.3×9.6×3.8 cm). The smaller configuration weighs about 326 g, runs on 5 V, and has an average power consumption of 4.5 W. In addition to the hardware reconfiguration, some changes to the GRID software were necessary in order for FOTON to navigate on orbit. The hardware and software changes that have been made are summarized in this section.
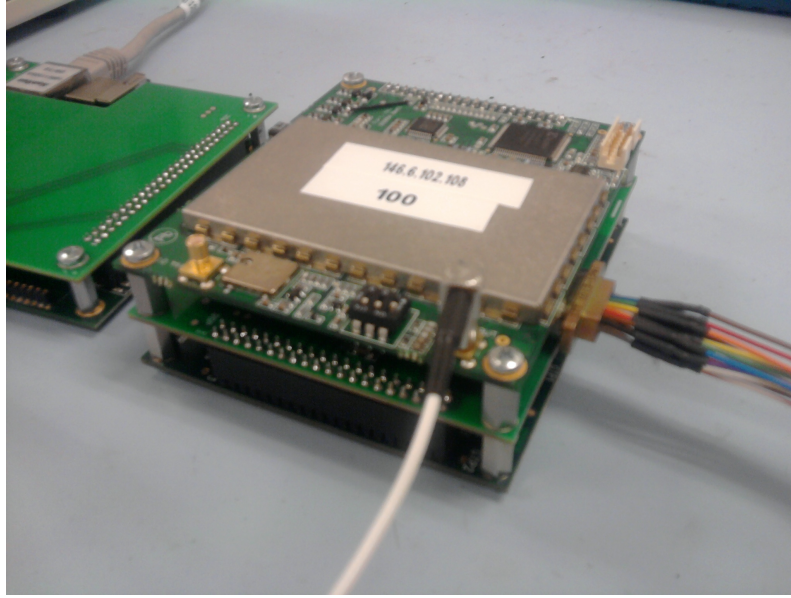
Figure 2.4: FOTON Receiver

### 2.4.1 Hardware Changes

The FOTON hardware consists of the same front end and DSP boards as CASES, but with a different interface board (the Z-board). The SBC board is not needed on FOTON, since the communication with the DSP will be handled directly by the satellite's on-board computer. The miniaturized three-board stack design, created by UT's Radionavigation Laboratory, is shown in Figure 2.4. The top board is the RF front end, the bottom is the DSP, and the middle board is the connecting Z-board. In addition to handling voltage conversion between the front end and DSP, the Z-board directs communication between the other two boards and a serial i/o port.

In the left of Figure 2.4 is a stand-alone SBC board (called the "jig" board). This is only used in testing as a user interface with FOTON in the absence of a satellite bus.

### 2.4.2 Software Changes

Because the GRID software was originally designed to run on a static, terrestrial receiver, several fundamental changes needed to be made before it could be used on FOTON. These software changes, like the hardware reconfiguration, were also made by the Radionavigation Laboratory.

The first change that needed to be made was widening the Doppler search window. Terrestrial receivers with TCXOs typically see up to 6 kHz Doppler, caused by the motion of the GPS satellite and the drift rate of the receiver's TCXO. The Doppler observed by receivers in LEO, however, is dominated by the receiver's dynamics, and can be as high as 40 kHz. Without widening the Doppler window, FOTON would not be able to track signals in LEO.

Another important change was in the navigation solution algorithm; because GRID was designed for static receivers, it uses a position averaging filter to attain sub-meter level accuracy. This must be turned off, however, for any dynamic scenarios, including LEO. Several other changes were made to the GRID in the process of making it space-capable, but as they were more general updates only indirectly related to FOTON, they will not be discussed.

# Chapter 3

# Characterization of CASES and FOTON

This chapter presents the initial characterization and development testing of the CASES and FOTON receivers. This not only illustrates how tightly coupled testing and development were in the project, but it also provides proper perspective for understanding the results of testing presented in later chapters. First, an overview of the testing setup and procedures is given, including a brief description of the hardware. Next, the results of testing the CASES receiver are presented; these act as a baseline for evaluating the performance of changes made to the code during early FOTON development. Finally, the initial characterization of the FOTON receiver is presented. The last test in this section is a recreation of the LEO benchmark test developed by Holt [8]. Thanks to the previously documented results of this same test on other receivers [9], FOTON's performance can be directly compared with other space-based receivers.

## 3.1    Setup and Procedures

There are two basic types of tests that were performed: live sky tests and simulations. Although some live sky testing is presented to verify that the receiver does, in fact, work properly with live data, the majority of testing presented used simulated signals. Simulations comprise static terrestrial, dynamic terrestrial, low earth orbit, and high earth orbit/geosynchronous (GEO)
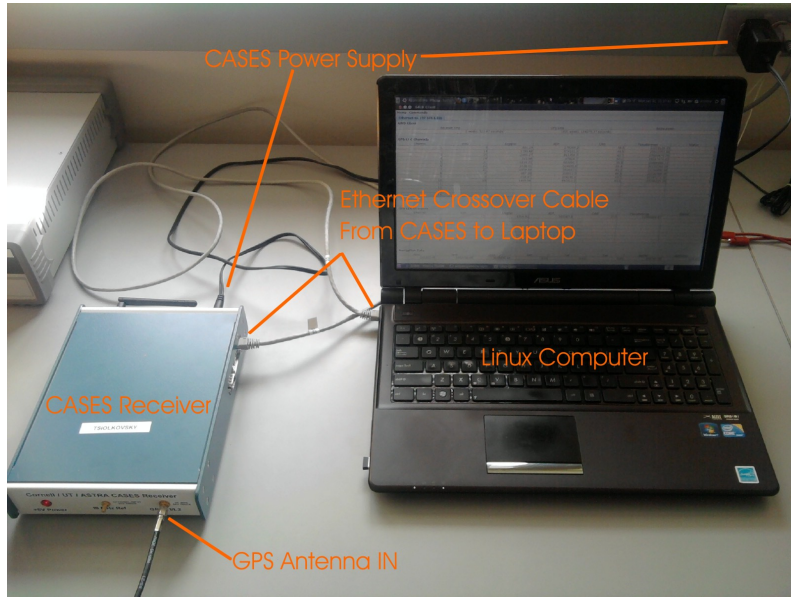
Figure 3.1: Live Sky Testing Setup

tests.

### 3.1.1 Live-Sky Testing

The live sky tests were conducted using a static GPS antenna on the roof of the W. R. Woolrich Laboratories building. The live sky testing setup is shown in Figure 3.1. The hardware required are a receiver (the CASES receiver is shown in the left side of Figure 3.1), a computer running a Linux operating system, an unobstructed antenna with a coaxial cable running to the receiver, and an Ethernet crossover cable for retrieving data from the receiver.

### 3.1.2 Simulator Setup

The Spirent GPS signal simulator is located at the Center for Space Research (CSR) GPS laboratory, and can be set up to simulate a variety of

scenarios, from a stationary receiver to a receiver in orbit. The simulation scenario is defined on an adjacent computer. Different parameters can be varied, including simulated antenna gain patterns and GPS constellation parameters. The simulator can also simulate atmospheric effects, such as ionospheric and tropospheric delay. The tests presented in this chapter, however, have these effects turned off. The simulator can also save a log file containing the "true" simulated position, velocity, and time, as well as satellite position and observables. Note, however, that what the simulator refers to as "pseudorange" includes only the transmitted part of the pseudorange; it cannot include the receiver clock bias.

The output of the simulator is the (nearly) analog signal that would be output from a receiver antenna, as defined in the simulation scenario. A coaxial cable connects the simulator's RF output to the receiver's antenna input (Fig. 3.2). It is sometimes necessary to use in-line amplification of the signal in between the simulator and the receiver; however, for the CASES and FOTON receivers it was sufficient to add a global gain offset to the signals in the scenario setup. A coaxial splitter is also used to input the same signal to a device called a "bitgrabber". The bitgrabber consists of a Bobyn front end (the same as FOTON's front end) connected to an Acces-IO USB-DI16A board data acquisition board [16]. This board transmits the digitized IF data from the front end through USB to a computer or hard drive for storage. Recording simulations in this way allows for quick testing of changes to the software without having to go back to CSR's GPS lab to re-run the tests.
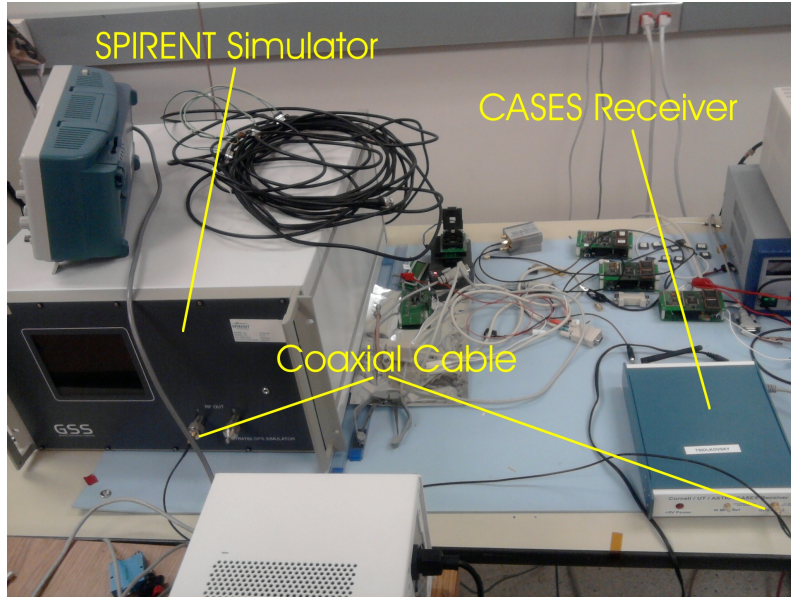
Figure 3.2: Spirent Simulator Setup

### 3.1.3 Simulator Testing Procedures

Before performing any dynamic tests with the simulator, the signal power must first be calibrated. There are several internal and external sources of signal power loss before the receiver (the coaxial splitter, for instance, has a 3.2 dB loss). This must be compensated for with either an in-line amplifier or a global signal power offset. An easy way to determine how much to compensate is to run a static scenario with the receiver connected, and compare carrier-to-noise ratios (C/No) with those observed during live-sky tests. Re-run the same static scenario, tuning the global signal power offset until the C/No ratio is close to the live-sky C/No.

Once the simulated power is tuned with a static scenario, other more complicated scenarios can be run. When the simulation is running, data is collected both from the receiver and from the bitgrabber. The final results

17
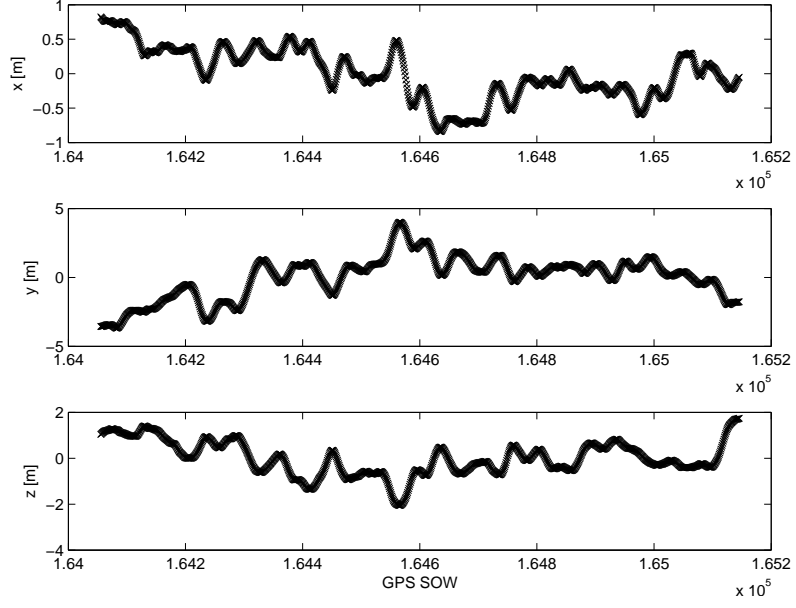
Figure 3.3: CASES Live-Sky Position Residuals

can be compared with the log file generated by the simulator.

## 3.2 CASES Receiver Testing

Before presenting the results of the FOTON characterization, three tests on the CASES receiver are presented: a live-sky test, a static simulation, and a LEO simulation.

### 3.2.1 Live-Sky Test

Approximately 20 minutes of live-sky data was recorded using the CASES receiver with the default GRID configuration. The average position and velocity over the 20 minute interval is subtracted to obtain approximate position and velocity residuals, shown in the following two figures.

18
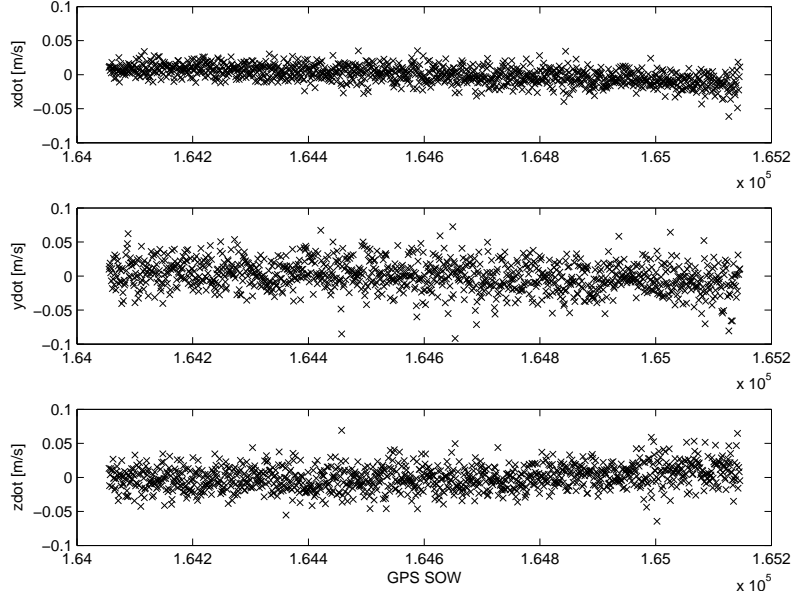
Figure 3.4: CASES Live-Sky Velocity Residuals

The default GRID configuration uses a position averaging filter to improve position precision over time; the effect of this filter is seen in Figure 3.3 as the position residuals "walk", rather than exhibiting Gaussian variations as do the velocity residuals (Fig. 3.4). The non-Gaussian behavior of the position residuals could alternatively be explained by multipath or some other time-correlated phenomenon; however, the averaging filter would most likely dominate other such effects. The 1-$\sigma$ error in position and velocity is summarized in Table 3.1. After only 20 minutes, the positioning error was less than 2 meters. Even greater precision is possible with longer position averaging times.

Table 3.1: CASES Live-Sky 1-$\sigma$ Error

|  | X | Y | Z | $\|\cdot\|$ |
|---|---|---|---|---|
| Position [m] | 0.377 | 1.541 | 0.744 | 1.753 |
| Velocity [m/s] | 0.013 | 0.022 | 0.017 | 0.031 |

### 3.2.2 Static Test

The static simulation scenario simulated the receiver at 30° N, 97° W, and included both ionospheric and tropospheric delays. Like the live sky test, the CASES receiver was used with the default GRID configuration, including the position averaging. The following figure shows the position filter converging toward the true solution over the course of the 2-hour simulation. The spikes in the plot result from changes in the tracked GPS satellites; this can be seen in Figure 3.6, which shows the 3D RMS error and position dilution of precision (PDOP) together. Also shown in this figure is the ratio of RMS error to PDOP, which is normally used to calculate user range error (URE). However, URE is based on the assumption of a normally-distributed position error; because of the position filtering, URE cannot be calculated.

### 3.2.3 LEO Test

The purpose of this test was to see how the GRID code, without any changes from the default configuration, would perform in a LEO scenario. The simulator was set up with a typical 90 minute low earth orbit (specifically that of the International Space Station [12]), and the simulation logging set to record the observables for all GPS satellites simulated. As expected, the receiver was not able to track enough satellites to obtain a navigation solution; however, it was able to track 1-3 satellites at a time. The primary tracking constraint was Doppler: GRID, by default, can only track Doppler on the
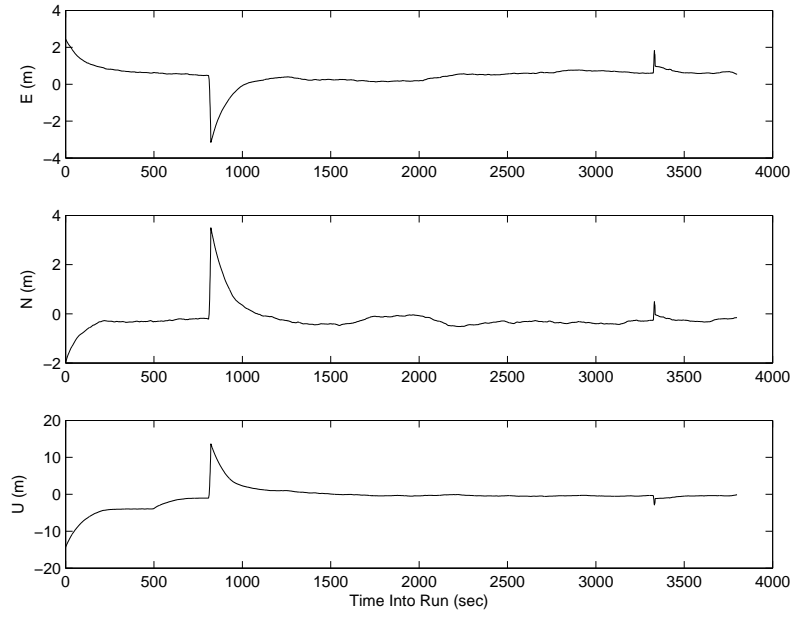
Figure 3.5: CASES Static Simulation Position Residuals
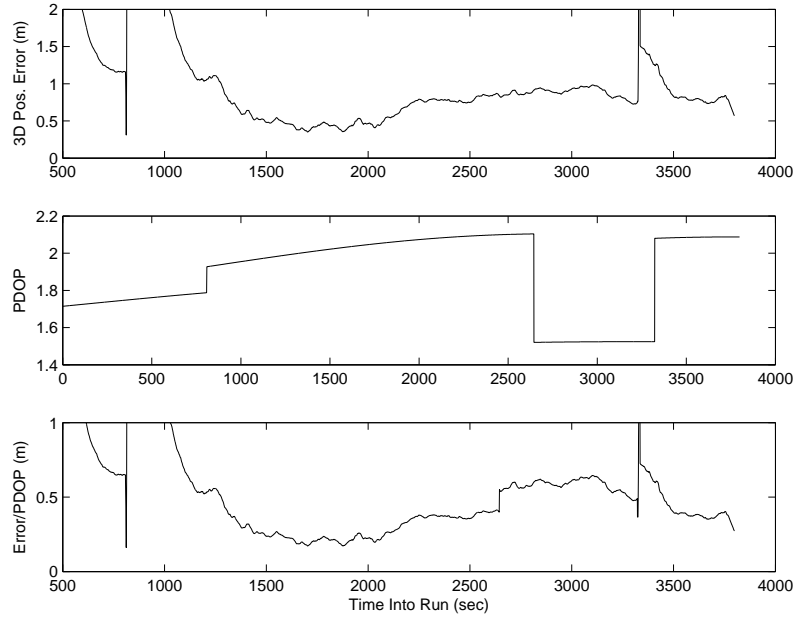


Figure 3.6: CASES Static Simulation RMS Error and PDOP

21
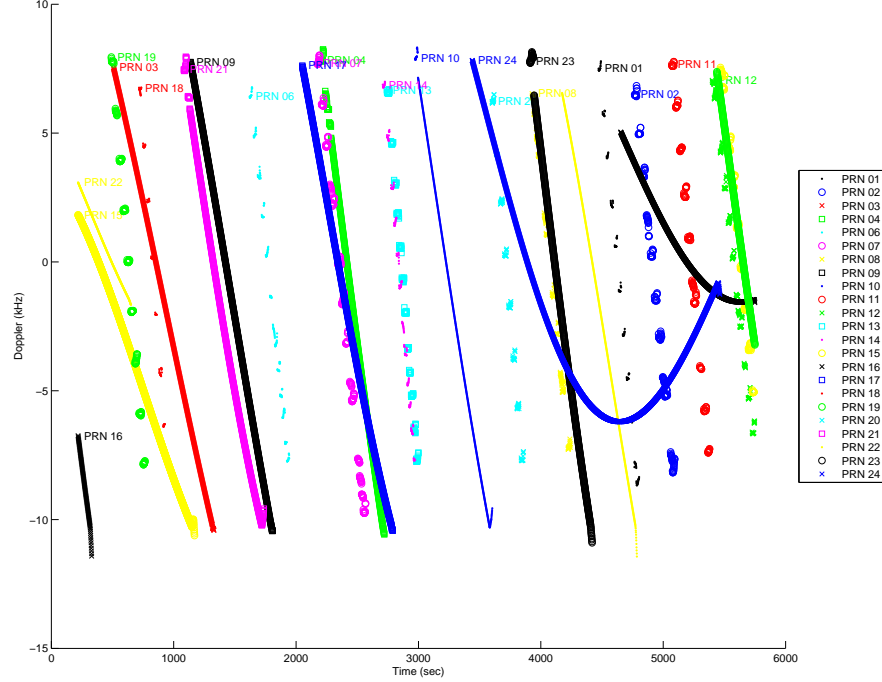
Figure 3.7: LEO Tracked Doppler History

range of +/- 10 kHz (see Fig. 3.7). Contrast this figure with the actual Doppler simulated (Fig. 3.8); the actual simulated Doppler is on the range of +/- 40 kHz.

## 3.3 FOTON Receiver Testing

After some required software changes to GRID, including the widening of the Doppler tracking window, the FOTON receiver was ready for testing. The first two tests were terrestrial: a static simulation and a simple rectangular track simulation. These tests were intended to verify that FOTON performed
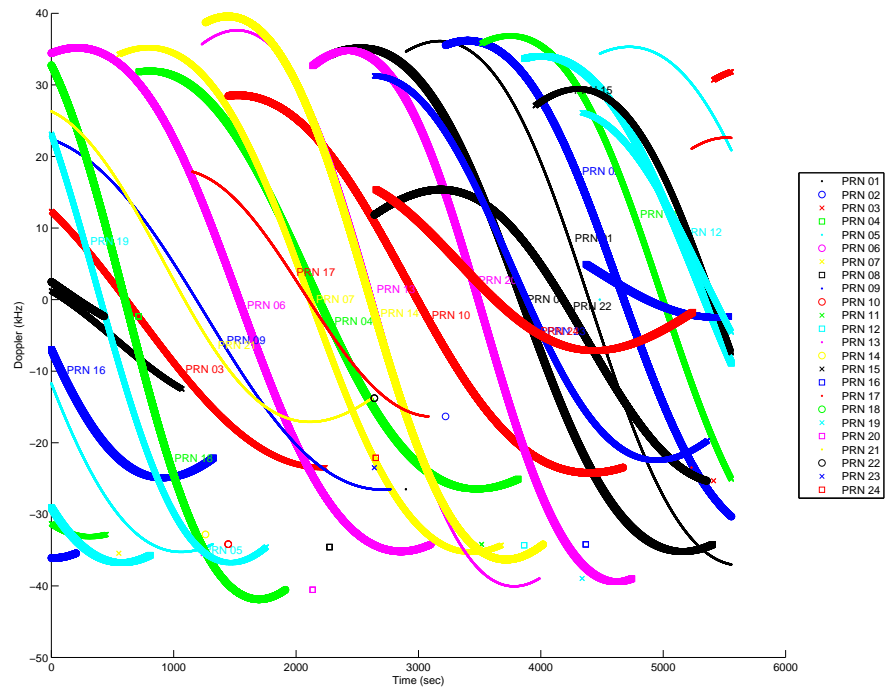
Figure 3.8: LEO Simulated Doppler History

as expected for a terrestrial receiver before attempting LEO positioning. These tests revealed a difference between the real-time receiver and PpRx, uncovering a bug in the SBC code, which was quickly located and fixed. Once the real-time receiver performed the same as PpRx, the code could be tested using an established LEO benchmark test. This test allows FOTON to be directly compared with other space-based GPS receivers, including the Orion single-frequency receiver used by small satellites in the past and the Jet Propulsion Laboratory's (JPL) dual-frequency BlackJack receiver, which has previously been used in major science missions.

### 3.3.1   Static Test

The static test was a repeat of the CASES static simulation, but without the atmospheric delays. Because this test is only used to demonstrate the basic functionality of the receiver, it was only 15 minutes long. The position and velocity residuals from the static simulation are shown in Figure 3.9. There was a 0.41 m overall bias in position, with a 0.46 m standard deviation. The velocity was zero-mean, with a 1-$\sigma$ error of 0.035 m/s.

### 3.3.2   Rectangular Track Test

The rectangular track test simulated the receiver traveling around a terrestrial track at velocities and accelerations typical of an automobile. This test demonstrates FOTON's capabilities to accurately track a receiver undergoing relatively slow terrestrial dynamics. Figure 3.10 shows the simulated trajectory in ECEF coordinates.

The ECEF position and velocity are shown component-wise in Figure 3.11. The thin line shows the actual simulated trajectory, while the thick line
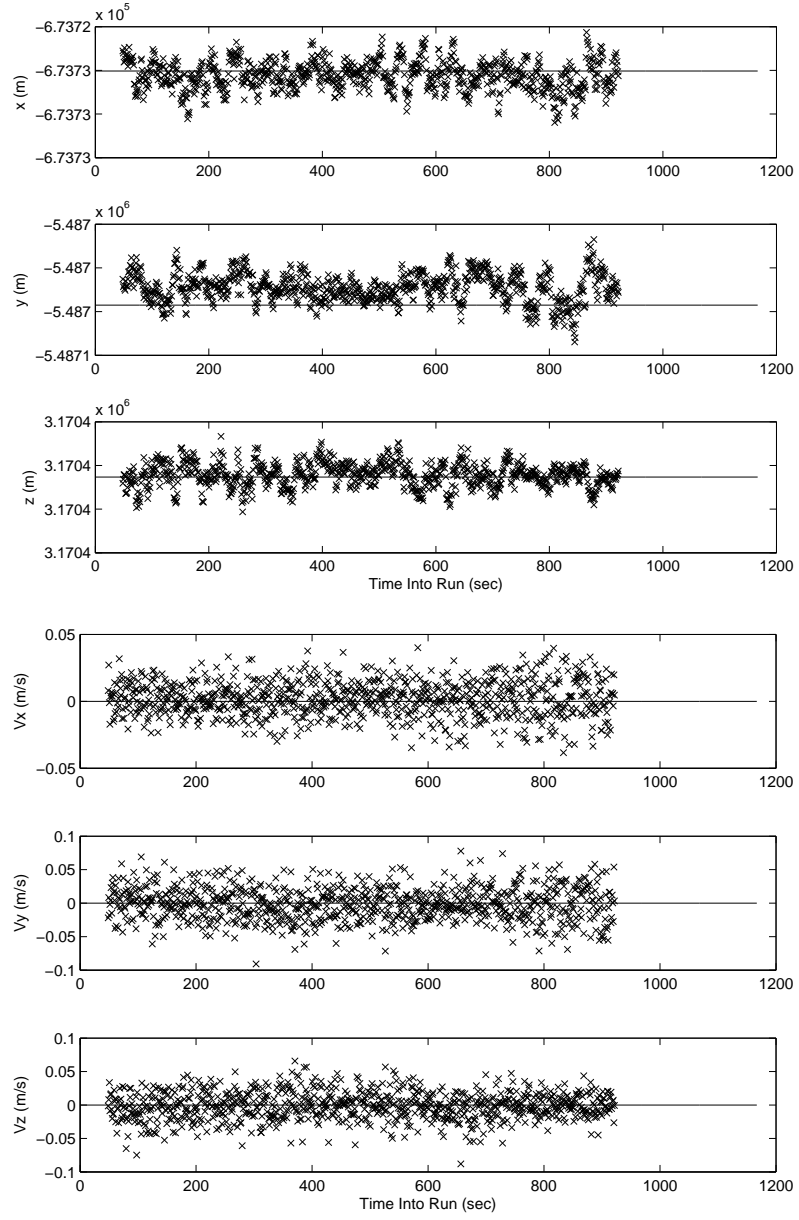
Figure 3.9: FOTON Static Simulation Residuals

25
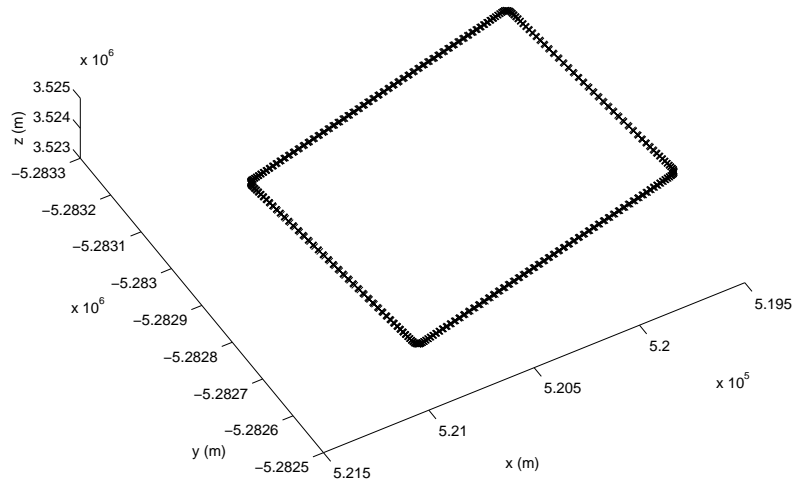
Figure 3.10: FOTON Rectangular Track Trajectory

shows FOTON's navigation solution. The associated RMS errors are shown in Figure 3.12. Both position and velocity were nearly zero-mean, with 1-$\sigma$ errors of 0.83 m and 0.12 m/s, respectively.

### 3.3.3 LEO Benchmark Tests

In 2002, Holt developed a LEO simulation specifically designed to test receiver performance under a variety of relative dynamics and signal levels [8]. The 2 hour simulation consists of a nearly polar orbit containing six pairs of GPS space vehicles (SVs) specifically chosen according to their relative dynamics and signal levels. The scenario begins at GPS week 1139, 172800 seconds of week; the orbit's Keplerian elements are listed in Table 3.2. This simulation uses L1 C/A only, and does not simulate ionospheric or tropospheric effects. It also does not include any ephemeris errors. By removing these

26
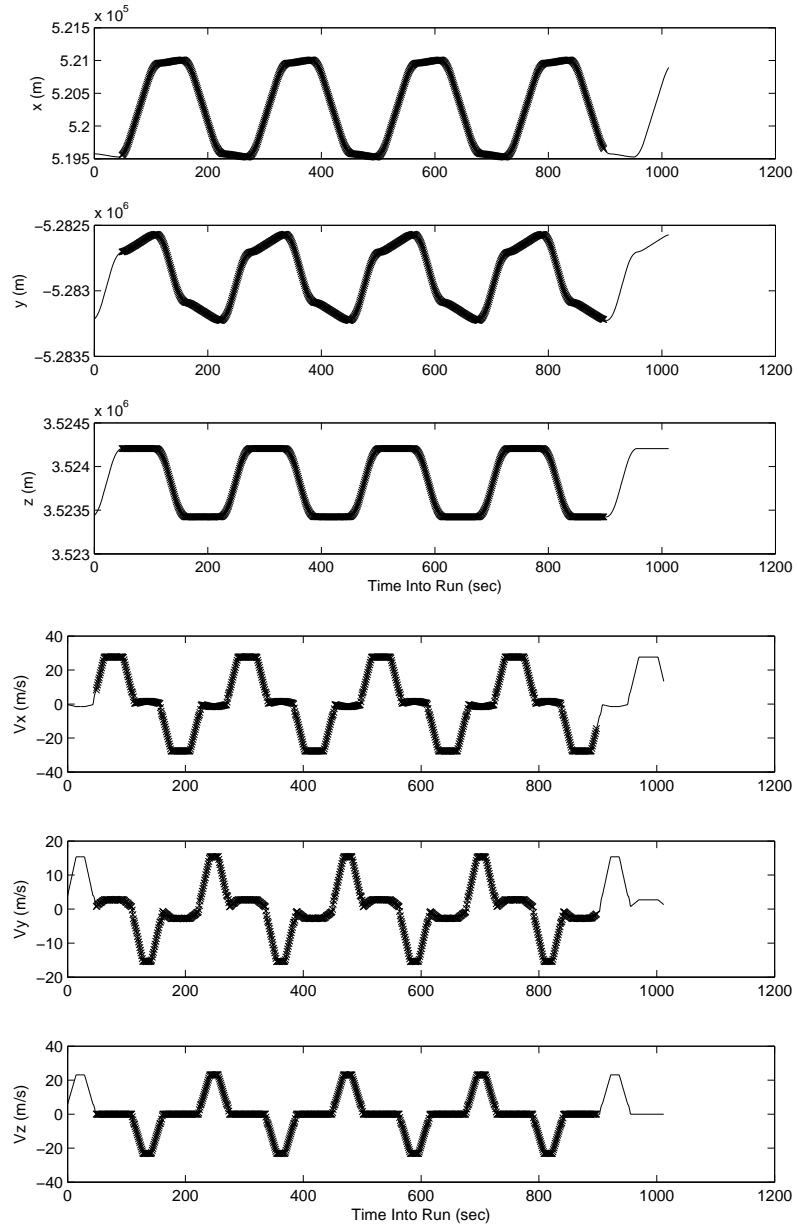
Figure 3.11: FOTON Rectangular Track ECEF Position and Velocity

27
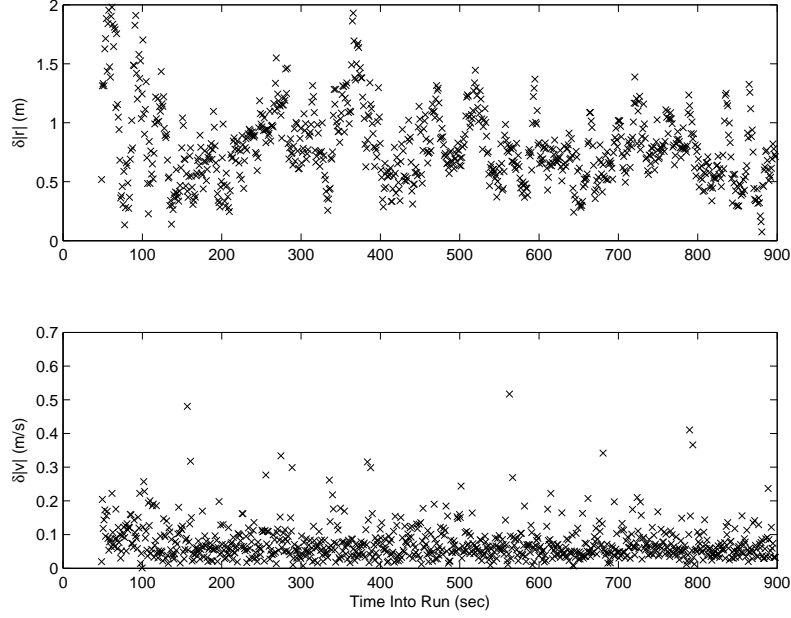
Figure 3.12: FOTON Rectangular Track RMS Errors

Table 3.2: Polar Orbital Elements

| SmA [km] | Ecc | Inc [deg] | RAAN [deg] | ArgP [deg] | MA [deg] |
|----------|------|-----------|------------|------------|----------|
| 6828 | 0.05 | 87 | 135 | 0 | 0 |

realistic sources of error, this simulation makes possible an analysis of raw observable noise.

The analysis consists of a series of double difference calculations using specified pairs of SVs and the "true" observables provided by the simulator log file. This process is illustrated in Figure 3.13. Because atmospheric delays are not simulated, the pseudorange, carrier phase, and Doppler (pseudorange rate) observables consist of only range, range rate, receiver and SV clock errors, and a constant phase ambiguity (modulo one wavelength). The first difference is between the computed observables and the simulator log file for each SV; this
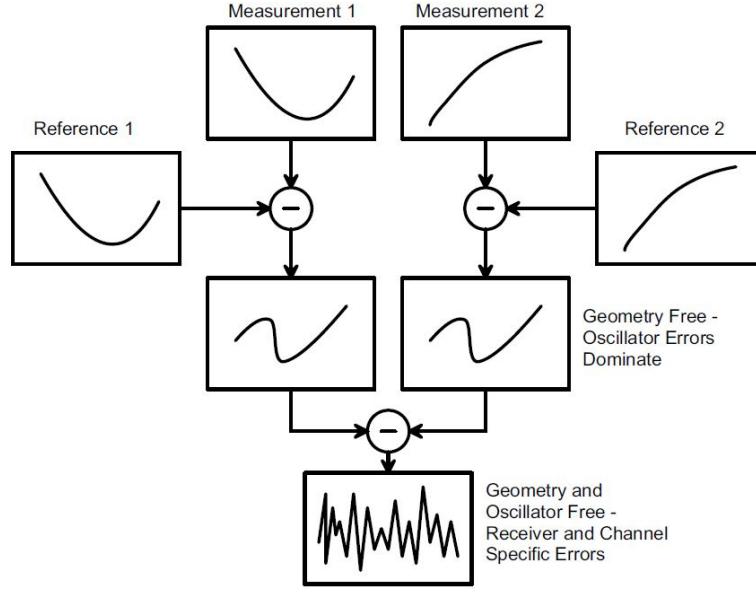
Figure 3.13: Observable Double Difference [8]

removes all terms except for the receiver clock errors and the phase ambiguity. The resulting differences are then differenced again, removing the receiver clock errors. All that remains is the observable noise, assumed to be zero-mean Gaussian, and the phase ambiguity. Since the phase noise is much lower than one wavelength (about 19 cm), the mean of the phase double difference, modulo one wavelength, can be subtracted out to obtain the zero-mean Gaussian phase error.

Note that it does not actually matter if the receiver-simulator differences are made first, or if the SV-SV differences are made first. However, in this analysis it will be assumed that the receiver-simulator differences are first, followed by an SV-SV difference. As an example, the carrier phase double

difference is outlined below:

$$\Delta\Phi^j = \Phi_{rx}^j - \Phi_{sim}^j$$
$$= c\delta t_r + \lambda N^j + n_\Phi^j \tag{3.1}$$
$$\Delta\Phi^k = \Phi_{rx}^k - \Phi_{sim}^k$$
$$= c\delta t_r + \lambda N^k + n_\Phi^k$$
$$\nabla\Delta\Phi^{jk} = \Delta\Phi^k - \Delta\Phi^j$$
$$= \lambda(N^k - N^j) + n_\Phi^k - n_\Phi^j \tag{3.2}$$
$$\sigma_{\nabla\Delta\Phi}^2 = \sigma_\Phi^2 + \sigma_\Phi^2$$
$$= 2\sigma_\Phi^2 \tag{3.3}$$

Here, $\Phi = \lambda\phi$ is the carrier phase expressed in meters, $N^j$ and $N^k$ are the integer phase ambiguities of SVs $j$ and $k$, respectively, and $n_\Phi^j$ and $n_\Phi^k$ are the observable noise terms. Note that it is assumed here that the simulator noise is negligible compared to that of the receiver, and that the receiver noise is independent of SV, so that the double difference noise is a factor of $\sqrt{2}$ greater than the actual observable noise. This is not strictly true, because the observable noise is dependent on received signal strength, but it is still a useful approximation. The only change in the above equations for the other observables is the integer ambiguities $N^j$ and $N^k$ are not present.

The six SV pairs are listed in Table 3.3, along with the times in which both SVs are visible to the receiver. The first three tests involve relatively low dynamics, while tests 3 and 6 involve relatively low signal level. Test 1 should be the easiest, because it involves a high signal level and low dynamics; test 6 should be the hardest, having high dynamics and low signal level.

The results from the last double difference test are shown in Figure 3.14 as an example; the remaining graphs are given in Appendix 1. Note the

Table 3.3: LEO Benchmark Test SV Pairs [8]

| Test | SV 1 | SV 2 | Start Time [sec] | End Time [sec] | Max Signal Level [dB] | Max. Rel. Accel. [g's] |
|---|---|---|---|---|---|---|
| 1 | 2 | 28 | 174000 | 175800 | 10 | 0.1 |
| 2 | 14 | 29 | 178100 | 180000 | 9 | 0.2 |
| 3 | 3 | 15 | 177400 | 178900 | 8 | 0.3 |
| 4 | 21 | 28 | 173900 | 174700 | 9 | 0.9 |
| 5 | 13 | 22 | 176500 | 177700 | 9 | 1.0 |
| 6 | 6 | 17 | 177100 | 178000 | 7 | 0.8 |

4 mm carrier phase bias; this bias is present in the last three (high-dynamics) tests, but not in the first two (low-dynamics) tests.

This bias can be explained by a small timing discrepancy. For instance, a 4 mm bias could be introduced to the pseudorange and carrier phase observables of an SV undergoing high dynamics (up to 40 kHz Doppler) if either the receiver or simulator clock was off by only 525 ns:

$$\delta\Phi \approx \dot{r}\Delta t \tag{3.4}$$

$$= f_D\lambda\Delta t \tag{3.5}$$

$$= (40 \times 10^6 \text{ Hz})(0.19 \text{ m})(525 \times 10^{-9} \text{ sec})$$

$$= 4 \text{ mm}$$

SVs undergoing low dynamics (up to 6 kHz Doppler) would not exhibit a noticeable bias in carrier phase. By shifting the receiver time (or alternatively, the simulator time) by 695 ns, this bias is eliminated, as shown in Figure 3.15; as expected, the carrier phase bias in the other high-dynamics cases is eliminated as well.

This 695 ns bias could be due to the receiver itself, or it could be a timing issue with the Spirent simulator. The simulator logs satellite data at 10
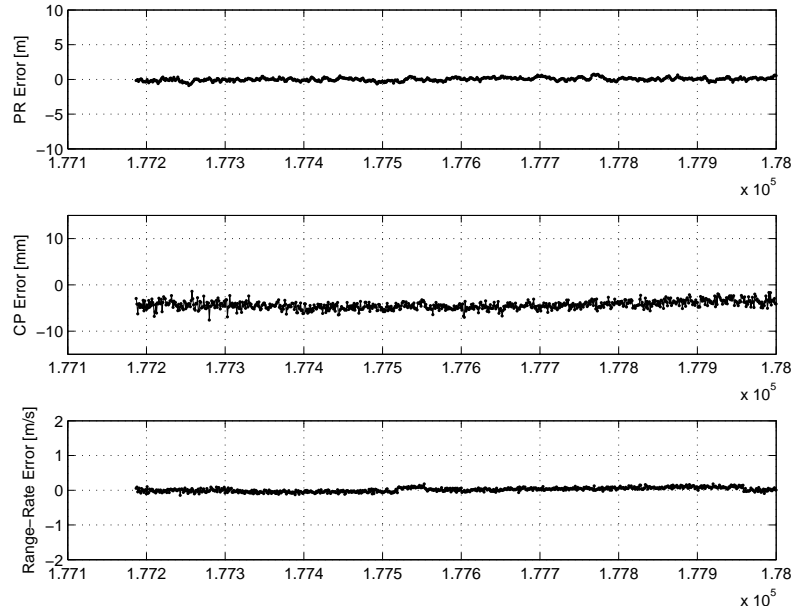
Figure 3.14: SV 6-17 Double Difference
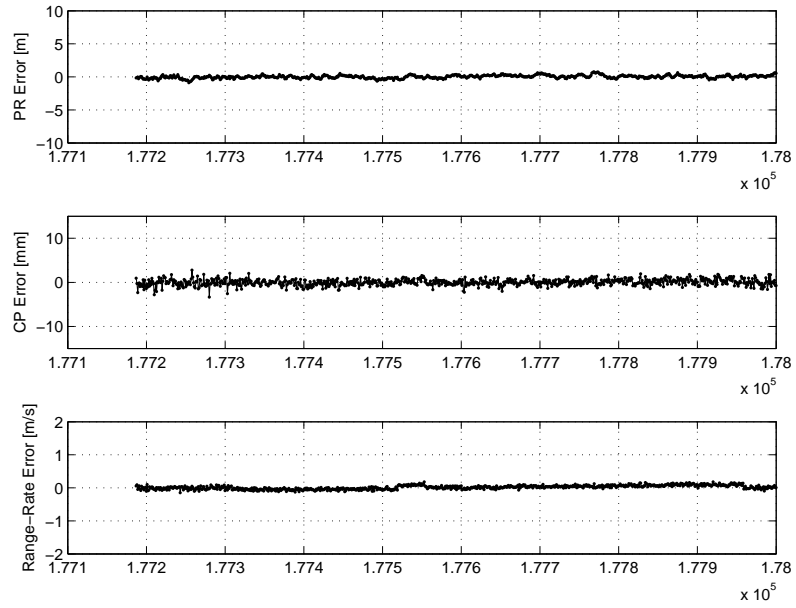


Figure 3.15: SV 6-17 Double Difference After Time Tag Fix-up

32

Hz, but, unlike the receiver, it time-tags the data with precision only matching the logging frequency (0, 0.1, 0.2, ...); it is possible that the simulator's time tags were simply truncated when inserted into the log file. Because Holt used the same simulator for his original tests in 2002, the simulator would have introduced similar biases into his data as well; however, because he produced zero-mean carrier phase double differences by subtracting out the mean rather than the mean modulo one wavelength, any systematic biases would be subtracted out. The only way then to determine if the problem is with the simulator would be to re-run these tests on a different receiver and look for the same bias.

The final test results, after the 695 ns time bias was removed, are summarized in Table 3.4. Note that test 3 is not shown; this is because the simulator log file did not include one of the SVs required by this test. Both SVs were simulated, as is evidenced by the fact that the receiver tracked both signals, however the log file only recorded a certain number of simulated SVs, and either SV 3 or 15 was not recorded between 177400 and 178900 seconds. This table shows that FOTON's performance is a significant improvement over the Architect and Orion receivers, though not quite as good as the BlackJack or NovAtel. These receivers, however, likely use time averaging of observables to improve performance, a technique not currently implemented on FOTON.

Table 3.4: LEO Benchmark Testing Observables Noise

| Test | Observable | FOTON | Architect | Orion | BlackJack | NovAtel |
|---|---|---|---|---|---|---|
| 1 | PR [m] | 0.1455 | 0.9258 | 0.9477 | 0.1553 | 0.0991 |
| | Phase [mm] | 0.5286 | 0.9323 | 0.9253 | 0.5030 | 1.1970 |
| | PR Rate [m/s] | 0.0503 | 0.1407 | 0.1414 | 0.0010 | 0.0745 |
| 2 | PR [m] | 0.1449 | 0.9037 | 0.9193 | 0.1025 | 0.1121 |
| | Phase [mm] | 0.5734 | 0.9227 | 1.0890 | 0.4270 | 1.2567 |
| | PR Rate [m/s] | 0.0537 | 0.1382 | 0.1440 | 0.0010 | 0.0359 |
| 3 | PR [m] | N/A | 0.9015 | 0.9559 | 0.1323 | 0.1226 |
| | Phase [mm] | N/A | 1.0899 | 1.0699 | 0.4105 | 1.3715 |
| | PR Rate [m/s] | N/A | 0.1419 | 0.1561 | 0.0010 | 0.0351 |
| 4 | PR [m] | 0.1548 | 0.9131 | 0.9029 | 0.1539 | 0.1267 |
| | Phase [mm] | 0.6805 | 1.1566 | 1.6478 | 0.9524 | 1.3559 |
| | PR Rate [m/s] | 0.0649 | 0.1526 | 0.1512 | 0.0010 | 0.0426 |
| 5 | PR [m] | 0.1708 | 0.8986 | 0.8960 | 0.1606 | 0.1217 |
| | Phase [mm] | 0.5784 | 1.1864 | 1.7767 | 0.6380 | 1.3480 |
| | PR Rate [m/s] | 0.0552 | 0.1469 | 0.1473 | 0.0010 | 0.0565 |
| 6 | PR [m] | 0.1920 | 0.9297 | 0.8942 | 0.1242 | 0.1285 |
| | Phase [mm] | 0.6255 | 1.2112 | 1.5659 | 0.2833 | 1.4228 |
| | PR Rate [m/s] | 0.0605 | 0.1466 | 0.1534 | 0.0010 | 0.0401 |
| Average | PR [m] | 0.1616 | 0.9121 | 0.9193 | 0.1381 | 0.1185 |
| | Phase [mm] | 0.5973 | 1.0832 | 1.3458 | 0.5357 | 1.3253 |
| | PR Rate [m/s] | 0.0569 | 0.1445 | 0.1489 | 0.0010 | 0.0475 |

# Chapter 4

# On-Orbit Acquisition and Reacquisition

In order to use FOTON on small satellites such as CubeSats, it is necessary to duty cycle the receiver due to power consumption constraints. While FOTON runs on an average of 4.5 W [1], a typical CubeSat has a total power budget of less than 10 W; it would not be feasible to use half of the total power for a single sensor. By only running FOTON for 1/3 of the time, however, its orbit-average power consumption can be reduced to 1.5 W. Since the receiver will only be active for short periods of time, it must be able to quickly acquire signals and begin reporting navigation solutions as soon as it is turned on. This chapter examines the time it takes to track enough signals to compute a navigation solution (time to first fix). In addition, several loss-of-signal scenarios are examined to show FOTON's signal reacquisition capabilities.

The scenario consists of the same polar LEO simulation used in the benchmark tests of Chapter 3. During the simulation, six events simulate various types of signal loss or duty cycling; each event is separated by several minutes of tracking to allow the receiver to fully recover a position solution. First, 6 minutes into the simulation, the simulated spacecraft performs a slow (6 minute duration) 360 roll. Next, the antenna is detached for 60 seconds, then reattached. Another roll is performed when the spacecraft is near the north pole, but this time a little faster (2 minute duration). The next two
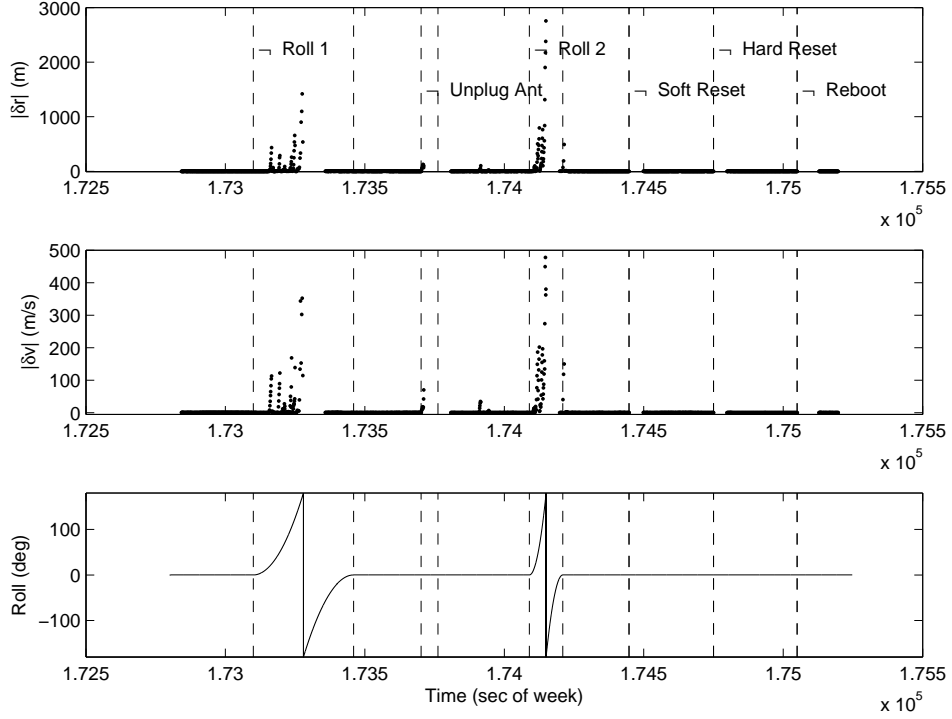
Figure 4.1: Acquisition Simulation Residuals

events are system resets, followed by a complete system reboot.

The six events are illustrated in Figure 4.1 as gaps in the navigation solution. Note the large increase in residuals for the 360° rolls (the 1st and 3rd events); this is due to the gradual degradation of receiver-satellite geometry during the rolls. The time history of these events is presented in Table 4.1.

## 4.1  Time to First Fix

The time to first fix is the time it takes for the receiver to obtain a valid navigation solution, measured from the moment the receiver is turned on. Time to first fix varies depending on DOP and acquisition search depth,

Table 4.1: Acquisition Simulation Event Times

| Event | Time | Event | Time |
|---|---|---|---|
| *6 Minute Roll* | | *2 Minute Roll* | |
| Begin | 300.0 | Begin | 1290.0 |
| Nav Lost | 485.5 | Nav Lost | 1349.5 |
| Track Lost | 500.5 | Nav Regained | 1398.5 |
| Track Regained | 511.5 | End | 1410.0 |
| Nav Regained | 558.5 | *Soft Reset* | |
| End | 660.0 | Cmd Reset | 1647.0 |
| *Detached Antenna* | | Track Regained | 1666.5 |
| Ant Detach | 902.0 | Nav Regained | 1698.5 |
| Nav Lost | 911.5 | *Hard Reset* | |
| Track Lost | 921.5 | Cmd Reset | 1950.0 |
| Ant Reattach | 962.0 | Track Regained | 1967.6 |
| Track Regained | 964.5 | Nav Regained | 1998.6 |
| Nav Regained | 1008.4 | *SBC Reboot* | |
| | | Cmd Reboot | 2250.0 |
| | | Track Regained | 2296.3 |
| | | Nav Regained | 2328.3 |

but on average, FOTON's time to first fix is about 45-50 seconds.

## 4.2 Six Minute Roll

The six minute roll began 5 minutes into the simulation. As can be seen in Figure 4.1, the receiver did not undergo a constant roll rate, but rather a more realistic spin-up and spin-down roll, with an average rate of 1 deg/sec. The receiver lost the navigation solution 185 seconds into the roll, and lost track of the last signal 200 seconds into the roll. In reality, the receiver could no longer see signals at at 180 seconds into the roll, because this was the half-way point when it was earth-pointing. However, the receiver continues to attempt to track signals that have disappeared until their low signal level identifies them as "ghost signals". FOTON reacquired the first signal on the later half of the roll at 211 seconds into the roll, that is, 31 seconds after the antenna was earth-pointing. The first valid navigation solution was obtained 47 seconds later; the total gap between valid navigation solutions was approximately 73 seconds.

## 4.3 Antenna Disconnect

Sudden loss of all signals was simulated by disconnecting the coaxial cable that connected the simulator to the receiver. This was done at a simulation time of 15 minutes, 3 minutes after the completion of the previous event. This 3 minute buffer ensured that the receiver had returned to normal operation. After the cable was disconnected, the receiver continued to track ghost signals for 20 seconds before they were all "pruned". After 60 seconds, the cable was reattached, and the receiver began tracking signals again 2 seconds

later. A valid navigation solution was obtained 44 seconds later.

## 4.4   Two Minute Roll

The two minute roll was started 21.5 minutes into the simulation, 5.5 minutes after the previous event. This time was chosen so that the receiver would be approximately at the north pole at the time of the roll (Fig. 4.2), so that in addition to the roll dynamics, the satellite geometry would be challenging as well. Because this roll was much quicker than the previous one (3 deg/sec average), the receiver never actually lost track on all satellites. It tracked ghost signals until real ones became visible. However, there was a 50 second gap in the navigation solution, from 1 minute into the roll (when the antenna was earth-pointing) to 10 seconds before the end of the roll. Even with the faster roll, however, the receiver still recovered a valid navigation solution before the roll was complete.

## 4.5   Soft and Hard Resets

Two reset commands can be issued to FOTON's DSP: a soft reset and a hard reset. Although this structure makes room for future functionality, at present both commands are exactly the same, and hereafter will be referred to simply as a reset. The next two events, again separated by 5 minutes to allow the receiver to fully recover, were a soft and hard reset, respectively. As expected, both commands performed the same DSP reset, and took the same amount of time. It took 17-18 seconds from the time the command was issued to regain tracking of the first signal, and another 30 seconds after that until the first valid navigation solution. The antenna-disconnect event
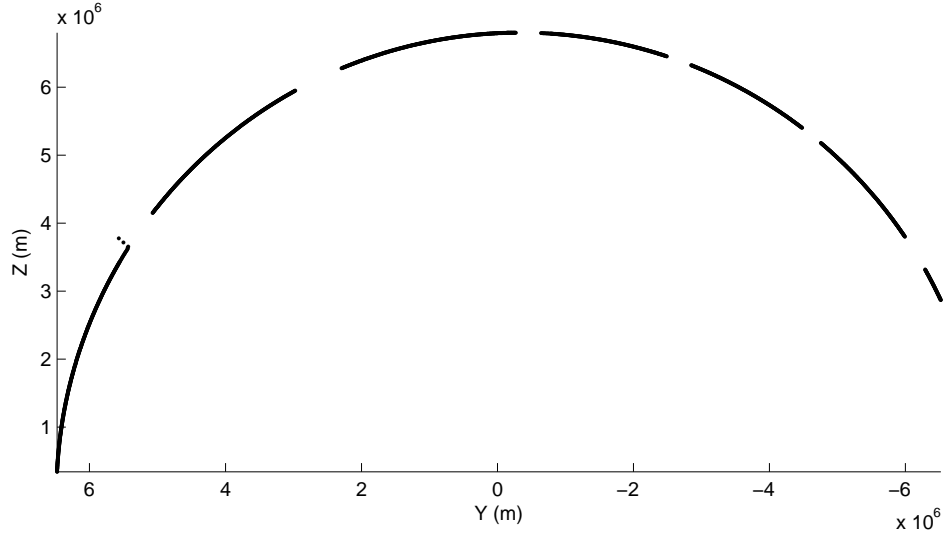
Figure 4.2: Acquisition Simulation Trajectory

demonstrated that the receiver only takes a few seconds to actually acquire a signal, so the reset time is then approximately 14-15 seconds.

## 4.6   SBC Reboot

Whereas the soft and hard resets only reset the DSP, a reboot actually shuts down the DSP and reboots the SBC. The reboot was commanded 5 minutes after the second DSP reset, and took about 46 seconds until the first signal was tracked, and another 32 seconds until the first navigation solution. Allowing 15 seconds for the DSP to reset, it takes about 30 seconds for the SBC to reboot.

## 4.7 Summary

FOTON's DSP only takes about 15 seconds to reset, after which it immediately begins acquiring new signals. Allowing 30-40 seconds for FOTON to acquire at least 4 valid L1 C/A signals, the time to first fix is still under one minute, which leaves ample on-duty time for active navigation.

# Chapter 5

# Kalman Filter-Based Precise Orbit Determination

The results presented until now have used a standard least-squares iterative solution based on the pseudorange and Doppler observables from each tracked SV [11]. In static scenarios, these basic point solutions can be averaged to improve overall precision. Similarly in dynamic scenarios, an Extended Kalman Filter (EKF) can be used to incorporate a time history of observables into a more precise navigation solution. This chapter outlines a basic orbital EKF for FOTON that improves on the default point solutions, making possible on-board, sub-meter precise orbit determination (POD) after a sufficient improvement of the dynamics model fidelity.

## 5.1 State Dynamics

The receiver's state consists of Earth-Centered, Earth-Fixed (ECEF) position $\mathbf{r}$ and velocity $\mathbf{v}$, and clock bias $\delta t_R$ and rate $\delta \dot{t}_R$:

$$\mathbf{x} = \begin{pmatrix} \mathbf{r} \\ c\delta t_R \\ \mathbf{v} \\ c\delta \dot{t}_R \end{pmatrix} \tag{5.1}$$

where the speed of light $c$ is used to express the clock terms in equivalent meters and meters per second (for unit consistency with the position and

velocity states). The receiver clock bias is defined as the difference between the receiver time and true GPS time (TGT):

$$\delta t_R = t_R - t_{GPS} \tag{5.2}$$

This EKF will be based on true GPS time rather than receiver time, so all time derivatives will be with respect to TGT.

The state differential equation model is then

$$\mathbf{f} = \dot{\mathbf{x}} = \begin{pmatrix} \mathbf{v} \\ c\delta \dot{t}_R + u_t \\ \mathbf{a} + \mathbf{u}_v \\ u_f \end{pmatrix} \tag{5.3}$$

where $\mathbf{a}$ is the total acceleration in the ECEF frame, and $\mathbf{u}_v$, $u_t$, and $u_f$ are uncorrelated, zero-mean, white-noise processes with covariances given by

$$\mathbf{Q}_v = E[\mathbf{u}_v \mathbf{u}_v^T] = \sigma_v^2 \mathbf{I}_{3 \times 3} \tag{5.4}$$

$$\sigma_t^2 = E[u_t(t)u_t(\tau)] = \frac{1}{2}h_0 c^2 \delta(t - \tau) \tag{5.5}$$

$$\sigma_f^2 = E[u_f(t)u_f(\tau)] = 2\pi^2 h_{-2} c^2 \delta(t - \tau) \tag{5.6}$$

Here, $h_0$ and $h_{-2}$ are constant parameters (units of sec and $\frac{1}{\text{sec}}$, respectively) used to characterize a receiver's clock stability [15], and $\delta(t - \tau)$ is the Kronecker delta function (units of $\frac{1}{\text{sec}}$). The velocity process noise $\sigma_v$ will serve as a filter tuning parameter.

The ECEF acceleration term in Equation 5.3 can be expressed in terms of the ECI acceleration:

$$\mathbf{a} = \mathbf{g} + 2\omega_e \begin{pmatrix} v_y \\ -v_x \\ 0 \end{pmatrix} + \omega_e^2 \begin{pmatrix} x \\ y \\ 0 \end{pmatrix} \tag{5.7}$$

43

where $\mathbf{g}$ is the total acceleration in the ECI reference frame. For now, a simple J2 gravity model [17] will be used, with no atmospheric drag, so that

$$\mathbf{g} = -\frac{\mu}{r^2}\left\{\left[1 + \frac{3}{2}\left(\frac{R_e}{r}\right)^2 J_2\left(1 - 5\left(\frac{z}{r}\right)^2\right)\right]\frac{\mathbf{r}}{r} + 2\left[\frac{3}{2}\left(\frac{R_e}{r}\right)^2 J_2\right]\frac{z}{r}\hat{\mathbf{k}}\right\}$$

(5.8)

where $\mu$ is Earth's gravitational parameter, $R_e$ is Earth's mean equatorial radius, $\hat{\mathbf{k}}$ is a unit vector along the +z-axis, and $J_2$ is the coefficient associated with the oblateness of the Earth.

### 5.1.1 Linearization

The state dynamics (Eqn. 5.3), linearized about the current best estimate of the state, $\hat{\mathbf{x}}$, can be written in state-space form as

$$\boldsymbol{\delta}\dot{\mathbf{x}} = \mathbf{A}(t)\boldsymbol{\delta}\mathbf{x} + \mathbf{Bu}$$

(5.9)

where

$$\boldsymbol{\delta}x \equiv \mathbf{x}(t) - \hat{\mathbf{x}}(t),$$

(5.10)

$$\mathbf{u} = \begin{pmatrix} u_t \\ \mathbf{u}_v \\ u_f \end{pmatrix},$$

(5.11)

$$\mathbf{A}(t) \equiv \left[\frac{\partial \mathbf{f}}{\partial \mathbf{x}}\right]_{\hat{\mathbf{x}}},$$

(5.12)

$$\mathbf{B} = \begin{pmatrix} \mathbf{0}_{3\times5} \\ \mathbf{I}_{5\times5} \end{pmatrix}$$

(5.13)

The constant $\mathbf{B}$ matrix will be used later to map the process noise variances to the state covariance. The system matrix $\mathbf{A}(t)$ is

$$\mathbf{A}(t) = \begin{pmatrix} 0 & 0 & 0 & 0 & 1 & 0 & 0 & 0 \\ 0 & 0 & 0 & 0 & 0 & 1 & 0 & 0 \\ 0 & 0 & 0 & 0 & 0 & 0 & 1 & 0 \\ 0 & 0 & 0 & 0 & 0 & 0 & 0 & 1 \\ & & & & 0 & 0 & 2\omega_e & 0 & 0 \\ & \frac{\partial \mathbf{a}}{\partial \mathbf{r}} & & 0 & -2\omega_e & 0 & 0 & 0 \\ & & & & 0 & 0 & 0 & 0 & 0 \\ 0 & 0 & 0 & 0 & 0 & 0 & 0 & 0 \end{pmatrix} \tag{5.14}$$

where

$$\frac{\partial \mathbf{a}}{\partial \mathbf{r}} = \frac{\partial \mathbf{g}}{\partial \mathbf{r}} + \begin{pmatrix} \omega_e^2 & 0 & 0 \\ 0 & \omega_e^2 & 0 \\ 0 & 0 & 0 \end{pmatrix} \tag{5.15}$$

and

$$\frac{\partial \mathbf{g}}{\partial \mathbf{r}} = \frac{\mu}{r^3} \left\{ \left[ 3 + \frac{15}{2} \left( \frac{R_e}{r} \right)^2 J_2 \left( 1 - 7 \left( \frac{z}{r} \right)^2 \right) \right] \frac{\mathbf{r}\mathbf{r}^T}{r^2} \right. \tag{5.16}$$
$$- \left[ 1 + \frac{3}{2} \left( \frac{R_e}{r} \right)^2 J_2 \left( 1 - 5 \left( \frac{z}{r} \right)^2 \right) \right] \mathbf{I}_{3\times3}$$
$$\left. + \frac{15}{2} \left( \frac{R_e}{r} \right)^2 J_2 \frac{2z(\hat{\mathbf{k}}\mathbf{r}^T + \mathbf{r}\hat{\mathbf{k}}^T)}{r^2} - \frac{3}{2} \left( \frac{R_e}{r} \right)^2 J_2 (2\hat{\mathbf{k}}\hat{\mathbf{k}}^T) \right\}$$

### 5.1.2 State Covariance Propagation

In order to propagate the state covariance matrix $\mathbf{P}$, the state transition matrix (STM) is needed. The most straightforward way of obtaining the STM is through direct numerical integration:

$$\dot{\boldsymbol{\Phi}}(t, t_0) = \mathbf{A}(t)\boldsymbol{\Phi}(t, t_0) \tag{5.17}$$
$$\boldsymbol{\Phi}(t_0, t_0) = \mathbf{I}$$

45

Once the STM is computed, it is used along with the previously defined process noise variances to propagate the state covariance [17]:

$$\mathbf{P}(t_k) = \mathbf{\Phi}(t_k, t_{k-1})\mathbf{P}(t_{k-1})\mathbf{\Phi}^T(t_k, t_{k-1}) + \mathbf{\Gamma}(t_k, t_{k-1})\mathbf{B}\mathbf{Q}\mathbf{B}^T\mathbf{\Gamma}^T(t_k, t_{k-1})$$
$$(5.18)$$

where

$$\mathbf{\Gamma}(t_k, t_{k-1}) \equiv \int_{t_{k-1}}^{t_k} \mathbf{\Phi}(t_k, \tau)d\tau \qquad (5.19)$$

and

$$\mathbf{Q} = \begin{pmatrix} \sigma_t^2 & \cdots & 0 \\ \vdots & \mathbf{Q}_v & \vdots \\ 0 & \cdots & \sigma_f^2 \end{pmatrix}_{5\times5} \qquad (5.20)$$

## 5.2   Measurement Models

This orbital EKF uses pseudorange and pseudorange rate observables in its measurement updates. While the pseudorange is a raw observable, the pseudorange rate is not; it is derived from Doppler. Since the only difference between pseudorange rate and Doppler is a constant scaling, however, the pseudorange rate is treated as a raw observable.

### 5.2.1   Pseudorange

The pseudorange model consists of the true range $r^k$ to the $k$th SV, the receiver clock bias $\delta t_R$, the SV clock bias $\delta t_S^k$, tropospheric $T^k$ and ionospheric $I^k$ delays, and noise $n_\rho^k$:

$$\hat{\rho}_k = r^k + c(\delta t_R - \delta t_S^k) + I^k + T^k + n_\rho^k \qquad (5.21)$$

46

Linearize this about the current best estimate of the state $\hat{\mathbf{x}}$:

$$\delta\rho_k = \rho_k - \hat{\rho}_k \tag{5.22}$$
$$= \mathbf{H}(t)\delta x(t)$$

where

$$\mathbf{H}(t) \equiv \left[\frac{\partial\hat{\rho}_k}{\partial\mathbf{x}}\right]_{\hat{\mathbf{x}}} \tag{5.23}$$
$$= \begin{pmatrix} \boldsymbol{\ell} & 1 & 0 & 0 & 0 & 0 \end{pmatrix}$$

and

$$\boldsymbol{\ell} \equiv \frac{\mathbf{r} - \mathbf{r}^k}{||\mathbf{r} - \mathbf{r}^k||} \tag{5.24}$$

is the line-of-sight vector from the SV to the receiver.

The noise in the pseudorange measurement can be estimated as a function of signal carrier-to-noise ratio $C/N_0$:

$$\sigma_\rho^2 = \frac{dB_{DLL}T_c^2c^2}{2\frac{C}{N_0}} \; [m^2] \tag{5.25}$$

where $d = \frac{t_{eml}}{T_c}$ is the DLL correlator's early-minus-late chip spacing, $T_c$ is the chip length (1 ms for GPS L1 C/A), and $B_{DLL}$ is the DLL bandwidth in Hz.

### 5.2.2 Pseudorange Rate

The pseudorange rate is derived from the Doppler observable as follows:

$$\dot{\rho} = -\lambda f_D = -c\frac{f_D}{f_0} \tag{5.26}$$

Where $f_0$ and $\lambda$ are the L1 frequency and wavelength, respectively, and $f_D$ is the observed Doppler shift of the received signal. The negative sign is

introduced because the Doppler shift is positive for approaching SVs, when the range rate is negative. A model for the pseudorange rate based on the current state involves the relative velocity $v_r$ along the line-of-sight vector $\boldsymbol{\ell}$, the receiver clock rate $\delta \dot{t}_R$, and the satellite clock rate $\delta \dot{t}_S$:

$$\hat{\dot{\rho}} = \left[ \frac{c \delta \dot{t}_R - c \delta \dot{t}_S - v_r(1 + \delta \dot{t}_S)}{(1 + \delta \dot{t}_S)(c + v_r)} \right] c \tag{5.27}$$

where

$$v_r = \boldsymbol{\ell}^T(\mathbf{v}^k - \mathbf{v}) = -\dot{r}^k \tag{5.28}$$

Again, linearize about the current state estimate:

$$\delta \dot{\rho}_k = \dot{\rho}_k - \hat{\dot{\rho}}_k \tag{5.29}$$

$$= \mathbf{V}(t) \delta x(t)$$

where

$$\mathbf{V}(t) \equiv \left[ \frac{\partial \hat{\dot{\rho}}_k}{\partial \mathbf{x}} \right]_{\hat{\mathbf{x}}} \tag{5.30}$$

$$= \begin{pmatrix} \frac{\partial \hat{\dot{\rho}}}{\partial \mathbf{r}} & 0 & \frac{\partial \hat{\dot{\rho}}}{\partial \mathbf{v}} & \frac{\partial \hat{\dot{\rho}}}{\partial c \delta \dot{t}_R} \end{pmatrix}$$

and

$$\frac{\partial \tilde{\dot{\rho}}}{\partial \mathbf{r}} = \frac{c(c + c\delta \dot{t}_R)}{(1 + \delta \dot{t}_S)(c + v_r)^2} \frac{1}{r} \left( v_r \boldsymbol{\ell} - (\mathbf{v}^k - \mathbf{v}) \right)^T \tag{5.31}$$

$$\frac{\partial \tilde{\dot{\rho}}}{\partial \mathbf{v}} = \frac{c(c + c\delta \dot{t}_R)}{(1 + \delta \dot{t}_S)(c + v_r)^2} \boldsymbol{\ell} \tag{5.32}$$

$$\frac{\partial \tilde{\dot{\rho}}}{\partial c \delta \dot{t}_R} = \frac{c}{(1 + \delta \dot{t}_S)(c + v_r)} \tag{5.33}$$

The noise in the pseudorange rate measurement can be estimated from carrier phase noise, a function of $C/N_0$, PLL bandwidth $B_n$, and the accumulation interval $T_{acc}$ (part of the squaring loss $S_L$ term).

$$\sigma_\phi^2 = \frac{B_n}{\frac{C}{N_0} S_L} \text{ rad}^2 \tag{5.34}$$

$$S_L^{-1} = 1 + \frac{1}{2 T_{acc} \frac{C}{N_0}} \tag{5.35}$$

Doppler can be approximated with a single-difference of phase, which leads to the pseudorange rate noise estimate.

$$f_D = -\frac{\dot{\rho}}{\lambda} \approx \frac{\phi_2 - \phi_1}{2\pi T_{acc}} \tag{5.36}$$

$$\dot{\rho} \approx -\frac{\lambda}{2\pi T_{acc}}(\phi_2 - \phi_1) \tag{5.37}$$

$$\sigma_{\dot{\rho}}^2 \approx \frac{2\sigma_\phi^2 \lambda^2}{(2\pi T_{acc})^2} \tag{5.38}$$

$$\sigma_{\dot{\rho}}^2 \approx \frac{2\lambda^2 B_n}{\frac{C}{N_0} S_L (2\pi T_{acc})^2} \text{ m}^2/\text{sec}^2 \tag{5.39}$$

## 5.3   EKF Results

The EKF was tested using the same polar LEO simulation as in previous sections. The EKF is initialized with the first point solution obtained (about 45 seconds into the simulation), with a diagonal initial covariance:

$$\mathbf{P}(t_0) = \begin{pmatrix} \sigma_{r0}^2 & & & & & & & \\ & \sigma_{r0}^2 & & & & & & \\ & & \sigma_{r0}^2 & & & & & \\ & & & \sigma_{t0}^2 & & & & \\ & & & & \sigma_{v0}^2 & & & \\ & & & & & \sigma_{v0}^2 & & \\ & & & & & & \sigma_{v0}^2 & \\ & & & & & & & \sigma_{f0}^2 \end{pmatrix} \tag{5.40}$$

49

with $\sigma_{r0} = \sigma_{t0} = 0.5\ m$ and $\sigma_{v0} = \sigma_{f0} = 0.1\ m/s$. These values are based on the approximate noise apparent in the standard point-wise navigation solution. The filter was tuned by varying the velocity process noise $\sigma_v$; the value that produced the best results was $\sigma_v = 0.001\ m/s^2$. The clock noise terms were calculated using $h_{-2} = 2.9 \times 10^{-21}\ sec^{-1}$ and $h_0 = 3.4 \times 10^{-21}\ sec$; these parameters were empirically computed by Kassas and Pesyna of the Radionavigation Laboratory for the TCXO used in FOTON's RF front end.

The position residuals are shown in Figure 5.1. Although the EKF noticeably reduces the noise in the position solution as compared with the point-wise solutions, it does not reduce the overall bias. This is because the EKF gravity model only includes J2 effects, whereas the simulator used a 10th order gravity model. The velocity, on the other hand, is nearly zero-mean, with an order-of-magnitude reduction of noise.

There is no way to directly measure clock error, so the best that can be done is to compare the clock bias and rate with the values obtained by the point-wise solutions computed at the same time. The difference in bias and rate (in equivalent meters and meters per second) is shown in Figure 5.2. It should be noted, however, that most of the noise shown is from the point solution; this can be seen in Figure 5.3, which shows the point-wise and EKF solutions for the clock rate. The EKF solution has much lower noise than the point solution. The results of the EKF vs. point solution comparison are summarized in Table 5.1.
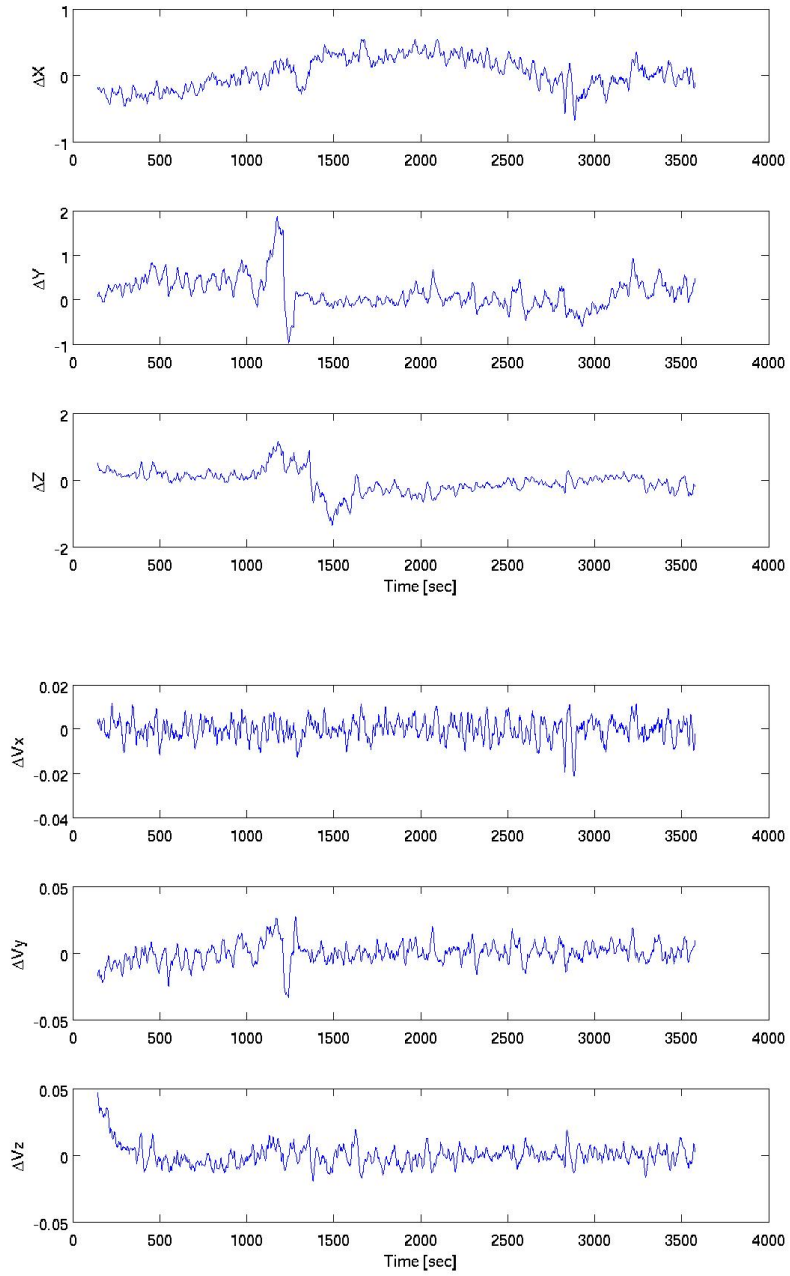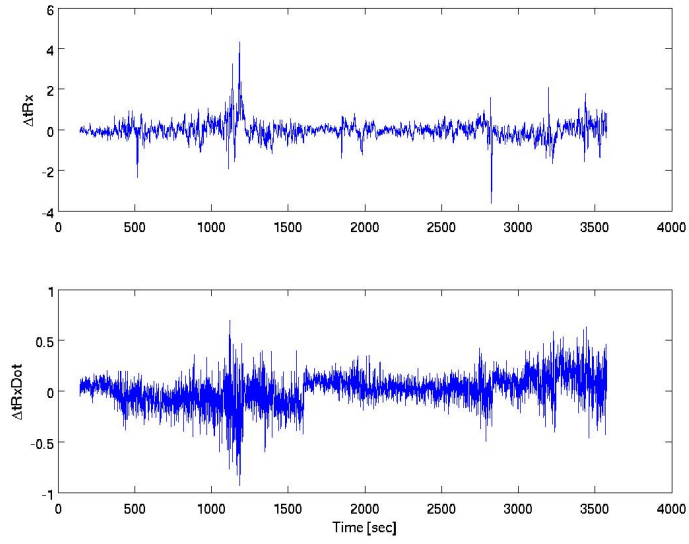
Figure 5.1: EKF Position and Velocity Residuals
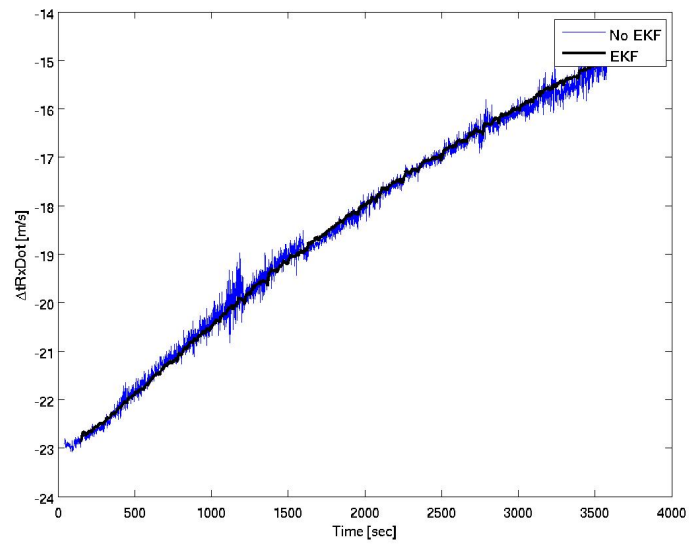
Figure 5.2: EKF - Point Solution Clock Residuals



Figure 5.3: EKF $c\dot{\delta t}_R$ Solution

Table 5.1: EKF and Point-Wise Residuals

| Solution | Position [m] | | Velocity [m/s] | | Clock | |
|---|---|---|---|---|---|---|
| Type | Mean | Std | Mean | Std | Bias | Rate |
| EKF | 0.174 | 0.544 | $1.22 \times 10^{-4}$ | 0.0121 | 0.432 m | 0.157 m/s |
| Point | 0.122 | 0.739 | 0.0812 | 0.247 | N/A | N/A |

# Chapter 6

# Dual-Frequency Capability

Designed specifically to be an ionospheric sensor, the CASES receiver was already set up to process dual-frequency measurements. Although FO-TON will also use its dual-frequency capability to directly measure ionospheric delay during satellite occultations, this chapter will focus on using the L2C signal to negate the effect of ionospheric delays to improve the navigation solution.

The Spirent simulator at UT-Austin that was used in previous tests is incapable of simulating L2C signals, so it could not be used for dual-frequency testing. Fortunately, Cornell University, one of the collaborators on the CASES receiver, has a newer Spirent device that does simulate L2C. O'Hanlon of Cornell used the newer simulator to record a dual-frequency, LEO simulation similar to the previously tested baseline polar orbit. In this simulation, L2C was simulated on all satellites. Currently, there are only 9 L2C-capable GPS satellites on orbit; however, the limited number of L2C-capable satellites can still be simulated by specifying in FOTON's configuration file which satellites to attempt to track. Also note that the simulated ionosphere was based on the standard Klobuchar model.

## 6.1   Interfrequency Bias

Due to slight differences in RF front end hardware, there is a hardware-dependent L1/L2 interfrequency pseudorange bias that must be calibrated and removed from the dual-frequency measurements. Suppose the true L1 and L2 pseudoranges $\rho_{L1}, \rho_{L2}$ were somehow known, the interfrequency bias can be computed as the difference in L1/L2 pseudorange residuals:

$$\Delta_{12} \equiv E\left[\delta\rho_{L1} - \delta\rho_{L2}\right] \tag{6.1}$$

$$= E\left[(\rho_{L1} - \hat{\rho}_{L1}) - (\rho_{L2} - \hat{\rho}_{L2})\right]$$

$$= E\left[(\rho_{L1} - \rho_{L2}) - (\hat{\rho}_{L1} - \hat{\rho}_{L2})\right]$$

where $\hat{\rho}$ is the measured pseudorange. It is impossible to know the true pseudoranges, but because the simulator used a Klobuchar ionospheric model, we only need the broadcast ephemeris to obtain the exact ionospheric delay according to the model. The ionospheric delay on the L1 frequency can also be expressed in terms of the L1 and L2 pseudoranges:

$$c\delta t_{Iono,L1} = \frac{f_{L2}^2}{f_{L2}^2 - f_{L1}^2}(\rho_{L1} - \rho_{L2}) \tag{6.2}$$

$$\rho_{L1} - \rho_{L2} = \frac{f_{L2}^2 - f_{L1}^2}{f_{L2}^2}(c\delta t_{Iono,L1}) \tag{6.3}$$

The interfrequency bias can then be written in terms of measured pseudoranges and ionospheric delay, computed from the Klobuchar model:

$$\Delta_{12} = E\left[\frac{f_{L2}^2 - f_{L1}^2}{f_{L2}^2}(c\delta t_{Iono,L1}) - (\hat{\rho}_{L1} - \hat{\rho}_{L2})\right] \tag{6.4}$$

After the GRID code was modified to print L1 and L2 pseudoranges, along with the computed Klobuchar model ionospheric delay, to a file, the dual-frequency LEO simulation was run, and the interfrequency bias computed
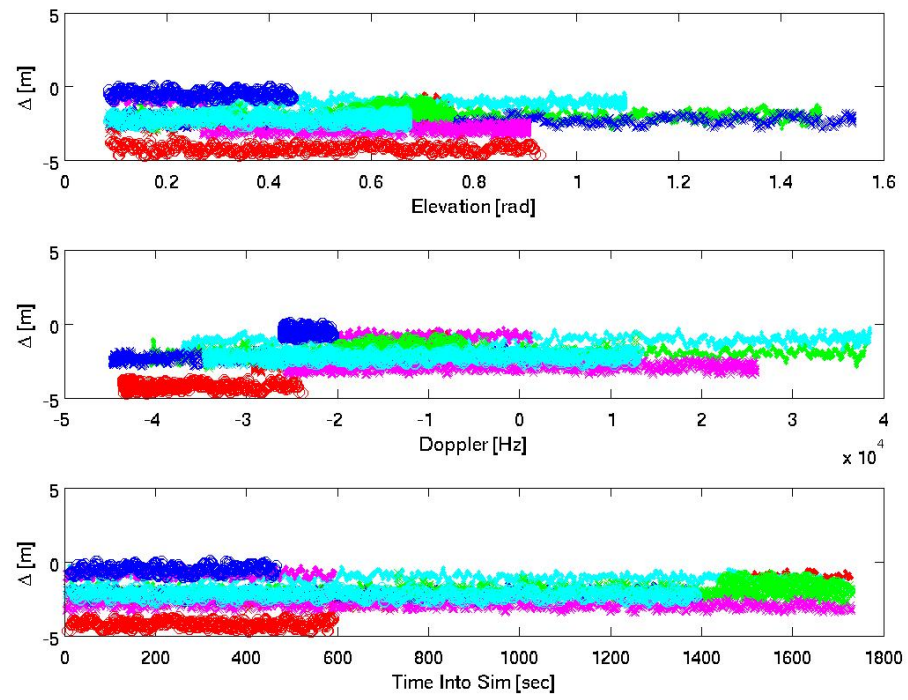
55

Figure 6.1: Interfrequency Bias

from the output file. Figure 6.1 shows the interfrequency bias for all tracked satellites for the duration of the simulation. Interfrequency bias is plotted against elevation and Doppler as well as time; this is done to make sure that the bias is independent of individual satellite characteristics. Although the bias on each satellite appears constant over the duration of the simulation, the bias is still different for each PRN. The cause of this has not yet been determined, but most of the bias can be eliminated by averaging over all satellites. The average interfrequency bias is -2.05 m, with a standard deviation of 0.86 m.

## 6.2 Dual-Frequency Ionospheric Delay Estimation

Most dual-frequency receivers directly eliminate the ionospheric delay for L2C-capable SVs by forming a measurement known as the "ionosphere-free" pseudorange:

$$\tilde{\rho}_{L1} = \rho_{L1} - \frac{f_{L2}^2}{f_{L2}^2 - f_{L1}^2}(\rho_{L1} - \rho_{L2}) \tag{6.5}$$
$$= \frac{f_{L1}^2 \rho_{L1} - f_{L2}^2 \rho_{L2}}{f_{L1}^2 - f_{L2}^2}$$

FOTON, however, does not use this ionosphere-free pseudorange. Instead, it uses the L1 and L2 pseudoranges from L2C-capable SVs to update a running estimate of vertical TEC (TECV). Satellite elevation is then used to map the TECV to a slant TEC for L1-only SVs as well as L2C-capable SVs. Not only does this method improve the estimate of ionospheric delay for L1-only satellites as well as L2C-capable ones, but it also acts as a filter on the ionospheric delay estimates, reducing noise. This works very well for stationary receivers (such as FOTON's predecessor CASES), but it may present problems for LEO receivers. For instance, while TECV changes slowly for stationary receivers, it

will change more rapidly for LEO receivers. In this case, independent, point-wise estimates of ionospheric delay may be more accurate, albeit more noisy, than filtered estimates.

## 6.3   LEO Simulation Testing

Once the interfrequency bias was determined, FOTON was tested using four different configurations. The baseline configuration (case 1) tracked L1 only, and initialized the Klobuchar model parameters with the actual parameters used in the simulation (also in the broadcast ephemeris). By initializing the Klobuchar parameters with the values used in the simulator from the beginning of the simulation, the receiver's ionospheric model is exactly matched with the simulator's model. This baseline case, then, should be more accurate than even dual-frequency configurations. Case 2 also tracked L1 only, but it initialized the Klobuchar parameters with the default null values; this demonstrates the receiver's default single-frequency performance in the presence of ionospheric delays. Case 3 tracked L1 and L2 on all satellites. This shows what performance can ultimately be expected as the GPS constellation is modernized. Case 4 also tracked L1 and L2, but restricts the L2 signals tracked to the 9 PRNs that currently transmit L2C. The results here presented were from the standard point-wise navigation algorithm; each case was also tested with the Kalman filter, but due to the low-fidelity dynamics model, sub-meter precision was not attained.

The position residuals from the case 1 are shown in Figure 6.2. Note the increase in noise near the end of the simulation; this was when the receiver was passing over the north pole, so DOP was higher.

Comparing this with case 2 (Fig. 6.3), the position residuals for the
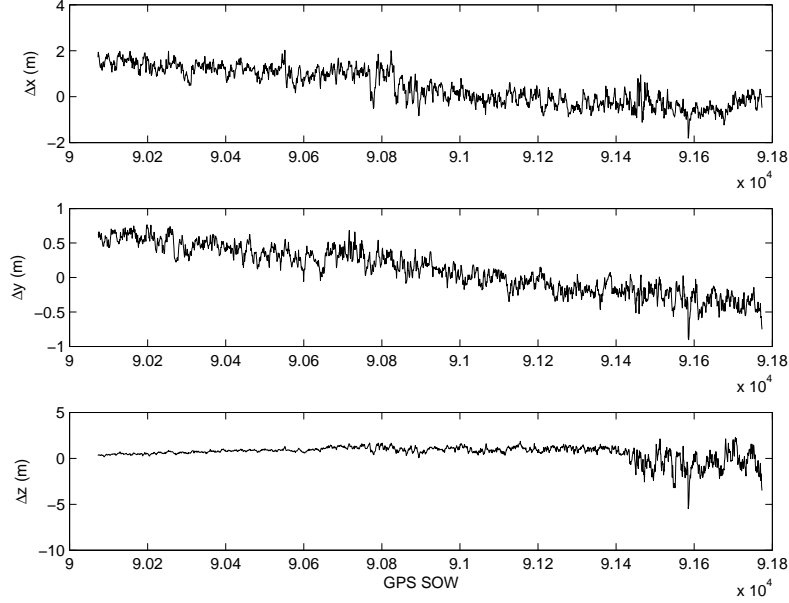
Figure 6.2: Position Residuals, L1-Only, Initialized Klobuchar Model (Case 1)

single-frequency configuration with uninitialized Klobuchar parameters, reveals a large initial error that is corrected about 8 minutes into the simulation. In this configuration, the Klobuchar model is initialized with null parameters, so the estimated ionospheric delay is zero. Once the Klobuchar parameters have been received from the broadcast ephemeris, however, the model is updated, and the ionospheric delays are properly estimated. After this correction, the residuals follow the same trends as the baseline configuration.

The position residuals for case 3 are shown in Figure 6.4. As expected, the errors are very similar to the baseline configuration (Fig. 6.2). Because of the way FOTON filters the L2C measurements to estimate the ionospheric delay for L1-only SVs as well as L2C-capable ones, the reduction in performance in case 4 (with limited number of L2C signals tracked) is minimal (Fig. 6.5).

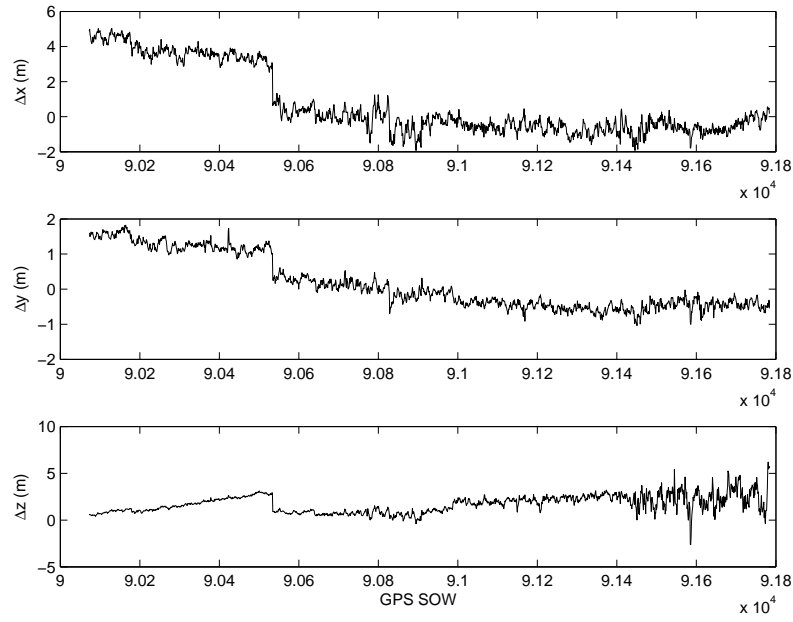Table 6.1 summarizes the position and velocity residuals for all four

59

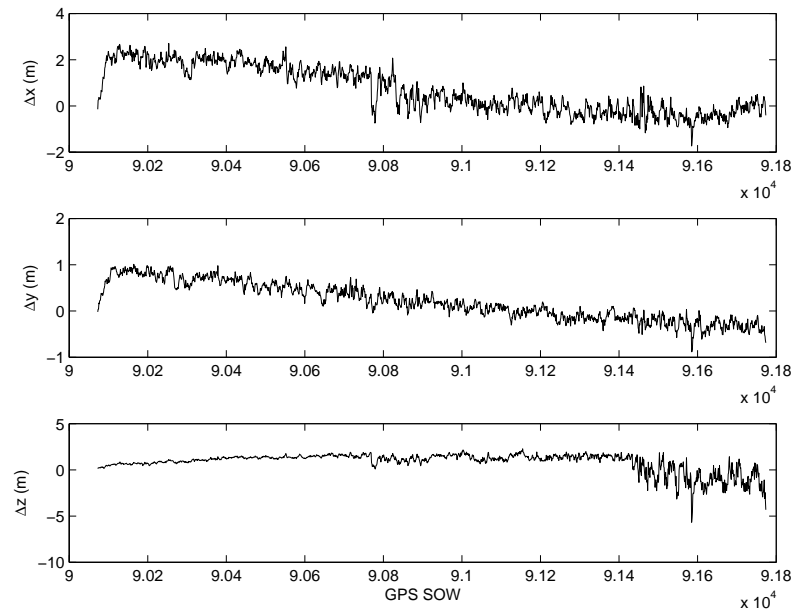Figure 6.3: Position Residuals, L1-Only, Uninitialized Klobuchar Model (Case 2)



Figure 6.4: Position Residuals, Dual-Frequency, All L2C (Case 3)
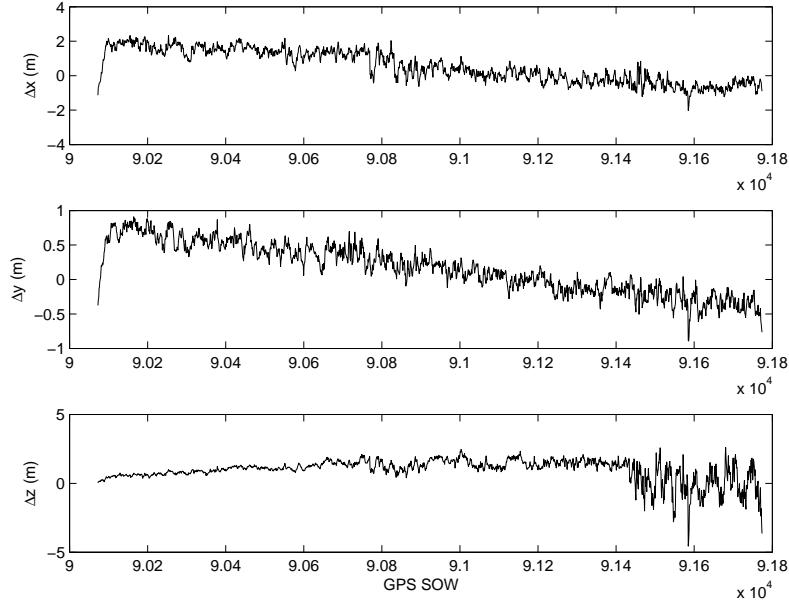
60

Figure 6.5: Position Residuals, Dual-Frequency, Limited L2C (Case 4)

configurations. As expected, the best configuration was the baseline; however, this is only because the receiver exactly matched ionospheric models with the simulator. The first half of case 2 is more representative of single-frequency performance. The two dual-frequency configurations were nearly identical; this is because of the filtering method currently employed to estimate the ionospheric delays. Note that the velocity residuals for all four configurations are essentially the same. This is because the standard point-wise navigation algorithm used in these tests computes velocity using Doppler only, and is independent of pseudorange, and thus ionospheric delay.

A comparison of these results with the single-frequency test results of Chapter 3 reveals a degradation in performance. This is clearly due to the presence of ionospheric delay on the pseudorange. However, sub-meter accuracy of the dual-frequency solutions is still attainable by including the raw

Table 6.1: Position and Velocity Point Solution Residuals

| | Position [m] | | Velocity [m/s] | |
|---|---|---|---|---|
| | Mean | 1-$\sigma$ | Mean | 1-$\sigma$ |
| L1, Init. Params | 0.7650 | 1.1520 | 0.0657 | 0.3035 |
| L1, Uninit. Params | 1.8520 | 2.2786 | 0.0661 | 0.3094 |
| DF, All L2C | 1.1040 | 1.4711 | 0.0628 | 0.2920 |
| DF, Limited L2C | 1.1190 | 1.2749 | 0.0612 | 0.3048 |

L2 pseudorange in a Kalman filter that is designed to process dual-frequency measurements. This capability, however, has yet to be developed.

# Chapter 7

# Radio Occultation Observation

In most terrestrial scenarios, GPS signals are received from relatively high elevation. In these cases, the signals travel through the ionosphere and troposphere more or less perpendicularly, passing through all of the layers before reaching the receiver. If the receiver is in LEO, however, it can track signals below the horizon; this happens as GPS satellites set behind the LEO satellite, because its velocity is much higher than that of the semi-synchronous GPS satellites. When this occurs, signals pass more horizontally through the ionospheric and tropospheric layers (Fig. 7.1); such an event is known as an occultation.

By using dual-frequency measurements, the slant total electron count (STEC or just TEC) along the signal path during an occultation can be directly computed. As the SV sets, the signal travels through more layers of the ionosphere, and the TEC increases. Complete TEC profiles during occultations can be used to map the ionosphere and monitor space weather. At low enough elevations, delay through the troposphere can also be calculated and used to compute density profiles, which can then be used to improve terrestrial weather models.

Several missions have been devoted entirely to radio occultations. The currently-operational COSMIC mission, for example, uses a small constellation of satellites with high-precision GPS receivers to observe occultations world-
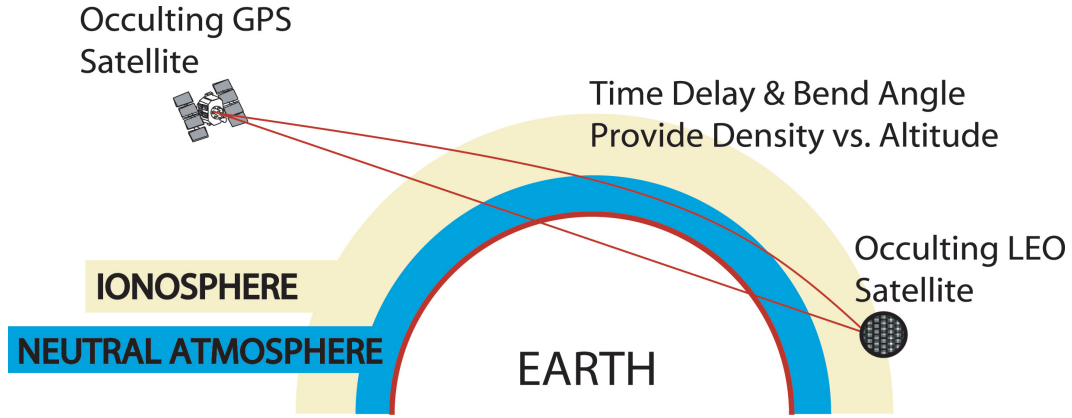
Figure 7.1: Radio Occultation [3]

wide [3]. With the small, low-power FOTON receiver, a similar mission could be performed with a larger constellation of much smaller CubeSats. Such a mission would provide even greater world-wide coverage than COSMIC at a fraction of the expense.

## 7.1 Occultation Observation in a LEO Simulation

The dual-frequency LEO simulation from Chapter 6 contains a number of occultations of varying elevations. To illustrate FOTON's occultation observing capability, the lowest-elevation SV tracked, PRN 13, was analyzed. FOTON acquired PRN 13 at an elevation of 78°, and tracked it until it set at an elevation of -15°. The slant TEC, computed with the pseudorange measurements, is the noisy measurement shown in Figure 7.2. The carrier-phase-derived TEC is the smooth line in this figure. Note, however, that carrier-phase-derived TEC is ambiguous, so it must be appropriately shifted to yield an accurate TEC measurement. If the pseudorange-derived TEC is denoted as $TEC_\rho$ and the carrier-phase-derived TEC relative to zero is denoted
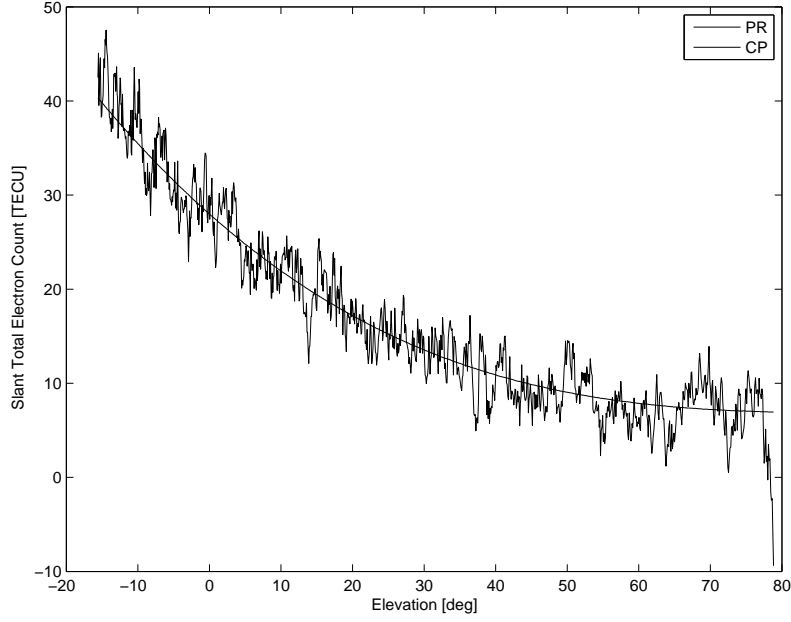
Figure 7.2: Slant TEC versus Elevation

as $\delta TEC_\Phi$, then the unbiased carrier-phase-derived TEC, denoted $TEC_\Phi$, is computed as

$$TEC_\Phi(t) = \delta TEC_\Phi(t) + E\left[TEC_\rho(t) - \delta TEC_\Phi(t)\right] \qquad (7.1)$$

Assuming a spherical Earth and a straight signal path through the ionosphere, the lowest altitude attianed by the signal can be computed from the elevation as follows:

$$h_{min} = r\cos(el) - R_e \qquad (7.2)$$

where $r$ is the norm of the LEO satellite's position, $R_e$ is the Earth's mean equatorial radius, and $el$ is the occulting SV's elevation. Note that these are
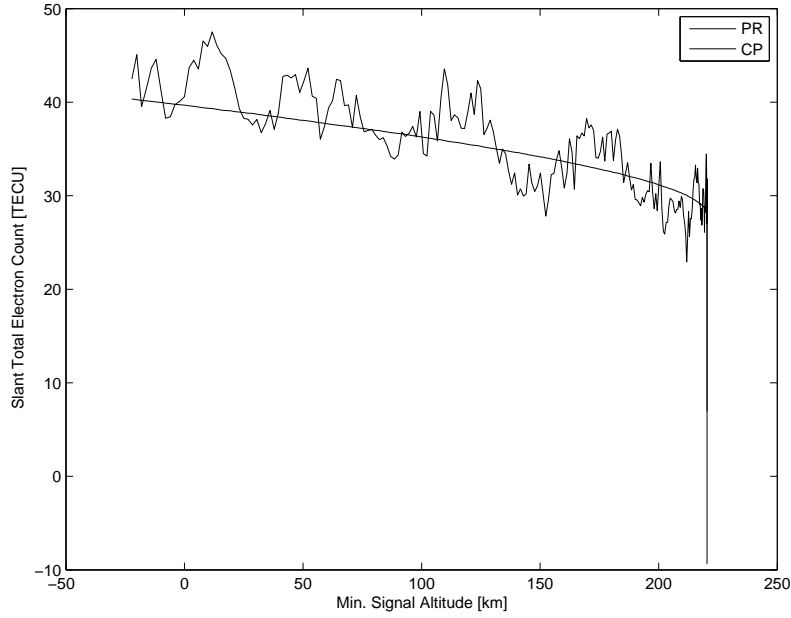
65

Figure 7.3: Slant TEC versus Altitude

not very good assumptions; the Earth is better modeled with an equatorial bulge, and the signal is bent as it travels through the ionosphere. However, these simplifying assumptions allows the elevation in Figure 7.2 to be mapped to altitude, shown in Figure 7.3, which illustrates that FOTON was able to track PRN 13 until it was blocked by the Earth itself.

This short example demonstrates that FOTON can be used effectively as an occultation sensor, even aboard a CubeSat. The relatively small expense of FOTON, combined with its small size and low power requirements, could make large-scale CubeSat occultation missions feasible.

# Chapter 8

# High Altitude and Geosynchronous Orbits

Up to this point, testing and development of FOTON has been based on the assumption that the receiver is in LEO. However, many satellites are placed in high Earth orbits (HEO), particularly geosynchronous (GEO). With a semi-major axis of 42164 km, GEO satellites are well outside the GPS constellation. Although GPS signals are directed toward the earth, the transmitters were designed with a slightly wider beam than is necessary for Earth coverage; as a result, a receiver in HEO or even GEO can still see some signals that are not blocked by the Earth (Fig. 8.1). In addition, the GPS transmitting antenna gain pattern includes some lower-power side lobes that may be possible to track. This chapter will present the results of preliminary GEO testing of the FOTON receiver.

## 8.1 GEO Simulation Setup

One challenge in setting up a GEO simulation is that, by default, the Spirent simulator assumes an isotropic transmitting antenna. This simplifying assumption is inconsequential for terrestrial or even LEO simulations, but it is unacceptable for GEO. Fortunately, the simulator is adaptable enough to allow the user to input a gain pattern for the transmitting antennae. The gain pattern used in the simulation is shown in Figure 8.2.
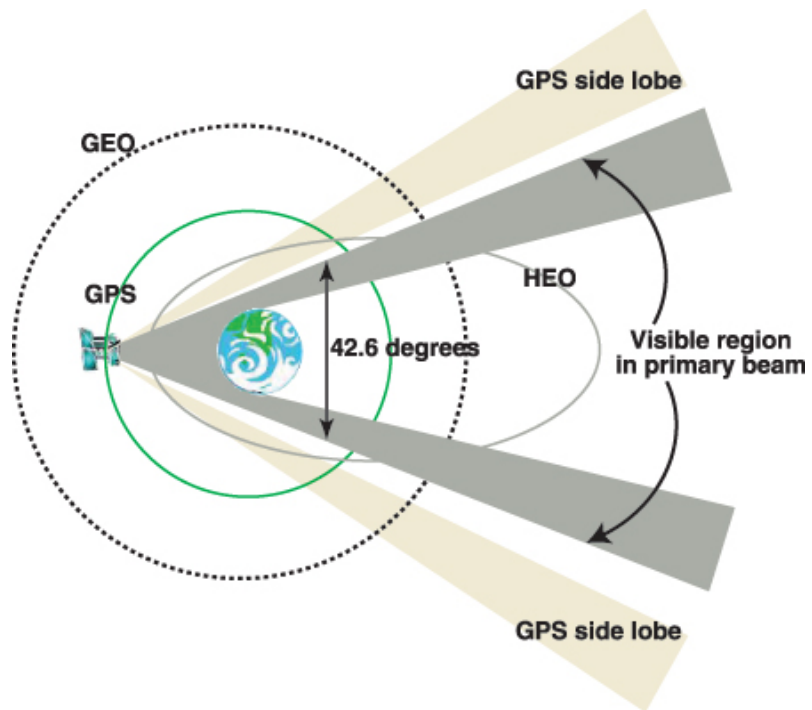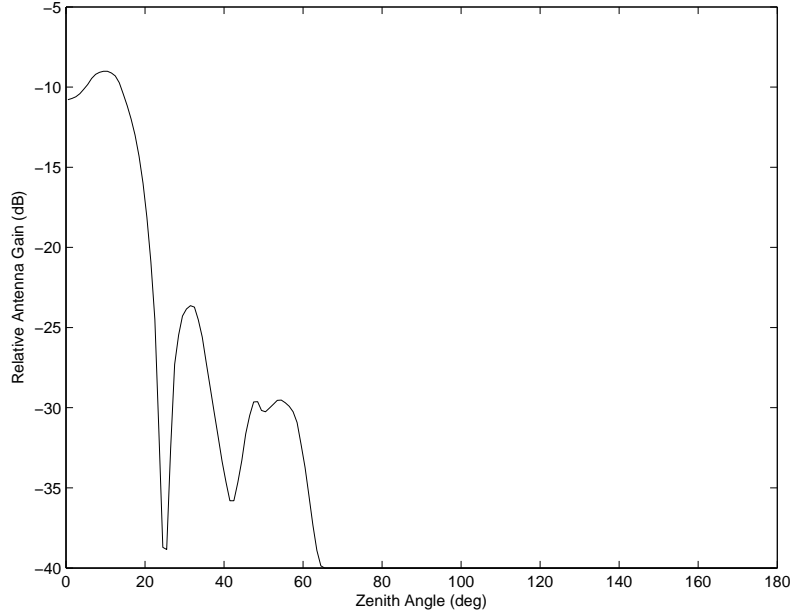
Figure 8.1: HEO/GEO GPS Geometry [6]

Figure 8.2: GPS Transmitting Antenna Gain Pattern [4]

As demonstrated by Moreau, the number of GPS satellites visible to a receiver in HEO/GEO is only occasionally four or more. Due to data storage limitations, a complete 24-hour simulation was not practical; instead, the GPS ephemerides for a specific epoch (in this case, week 1139, 172800 seconds of week) were propagated for 24 hours, and a two-hour window containing at least four visible satellites was selected. This window began at 244800 seconds of week 1139. Before running the simulation, however, the overall transmission gain was adjusted as described in the simulation testing procedures. This ensures an accurate modeling of the GPS signal strength.

Unlike the previous tests in which FOTON used its own internal TCXO clock, this time the receiver was slaved to an external OCXO. This more stable clock allows a reduction in the PLL bandwidth, which decreases the signal noise. This increases the received $C/N_0$, which is essential to tracking weak

signals in GEO.

## 8.2 Point-Wise Solutions

In order to acquire and track the weak signals expected in GEO, FO-TON was configured to perform 20 ms coherent accumulation; this is the maximum allowable accumulation interval without using data bit wipe-off techniques. In addition, the Doppler search window was reduced to +/- 10 kHz because the receiver is expected to be stationary (in the ECEF frame). Finally, the PLL bandwidth was also reduced to 10 Hz, further decreasing noise levels.

As anticipated, the receiver tracked four signals for most of the two-hour simulation. The number of satellites tracked is shown in Figure 8.3; it varied from two to four SVs. During the times when the receiver tracked four satellites it was able to compute a navigation solution using the standard point-wise algorithm. Given the fact that DOP is one to two orders of magnitude higher in GEO, the residuals of these point solutions are relatively small (Figs. 8.4 and 8.5).

The already bad geometry appears to get even worse towards the end of the simulation (after 5000 seconds), but for the first two periods of four-SV-visibility, the navigation solution is relatively good. The error along the X-axis (the radial direction) is far worse than the errors in the Y-Z horizontal plane. This is no surprise given the lack of geometric diversity in the X-direction. The errors for these first two data sets are given in Table 8.1.
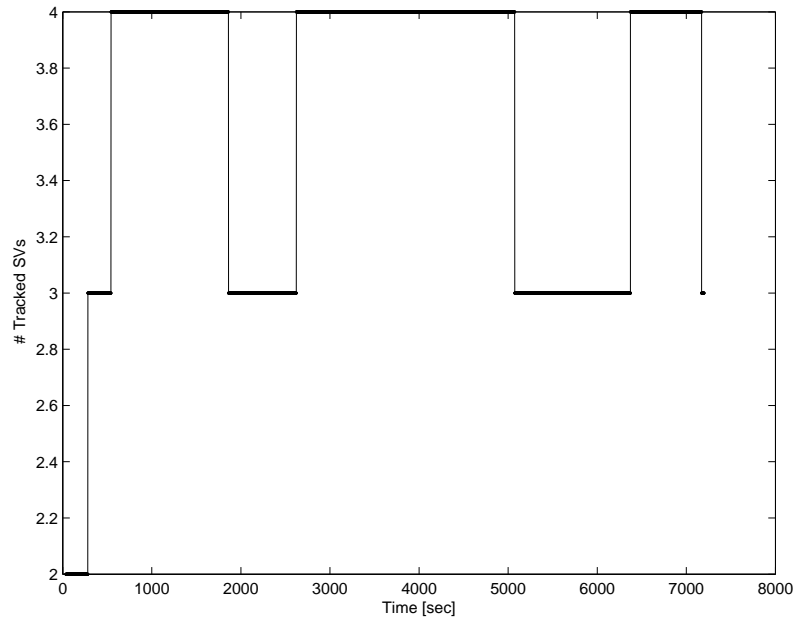
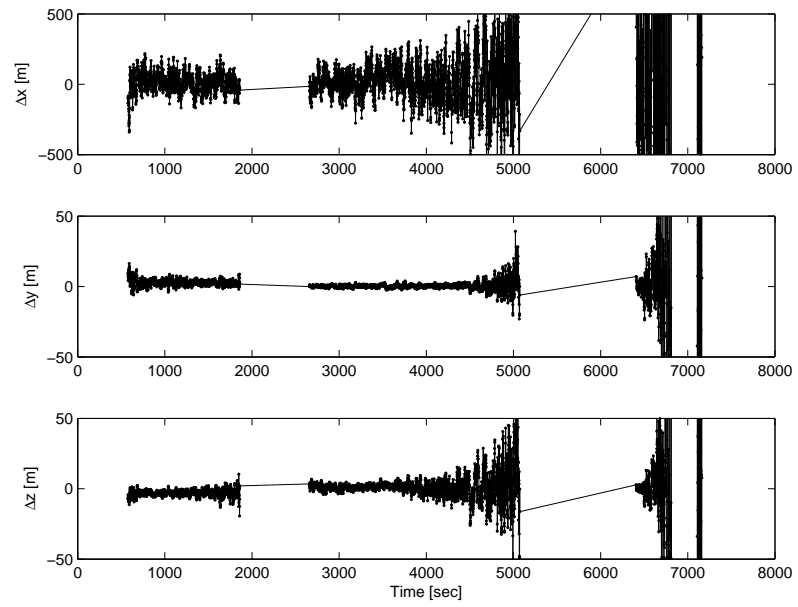Figure 8.3: Number of Satellites Tracked
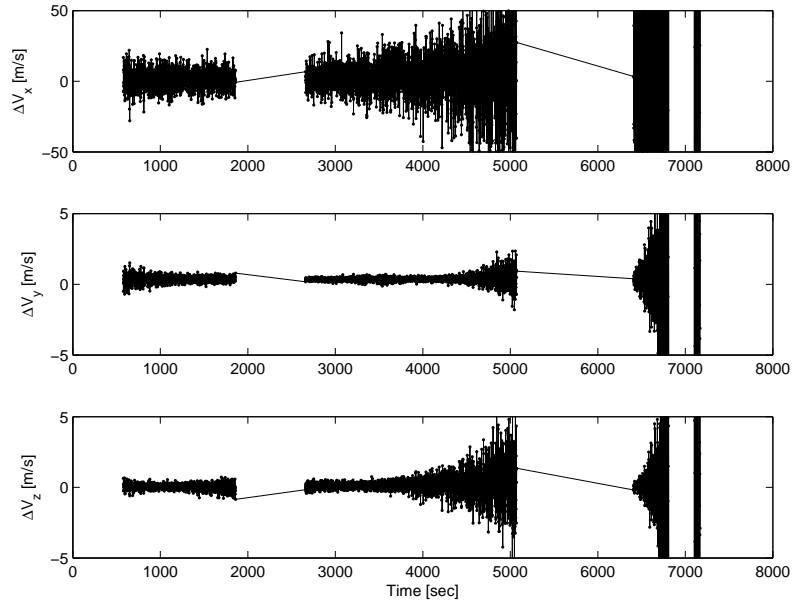


Figure 8.4: GEO Position Residuals

71

Figure 8.5: GEO Velocity Residuals

Table 8.1: GEO Navigation Solution Residuals

|          | X        | Y       | Z       | $\|r\|$  |
|----------|----------|---------|---------|----------|
|          | Position [m] | | | |
| Mean:    | 18.281   | 1.276   | -0.145  | 18.326   |
| 1-$\sigma$: | 155.3673 | 3.1213  | 7.9116  | 155.5999 |
|          | Velocity [m/s] | | | |
| Mean:    | 2.3692   | 0.3665  | 0.1286  | 2.4008   |
| 1-$\sigma$: | 14.92136 | 0.26513 | 0.68159 | 14.93927 |

## 8.3 Summary

By using an external OCXO to allow smaller a PLL bandwidth and using longer coherent accumulation time to increase signal $C/N_0$, FOTON is able to determine horizontal position in GEO to within 10 meters, and vertical position within 200 meters, without the need of filtering. A properly tuned Kalman filter would further enhance performance. Furthermore, due to the low signal dynamics present in GEO, even longer coherent accumulation times may be used, provided the data bits are wiped off appropriately. This will allow FOTON to pull in signals from transmitter side lobes in addition to the main lobes, making more SVs visible, and further increasing GEO navigation performance.

# Chapter 9

# Conclusion

As satellites shrink in size and grow in navigation requirements, the need for a small, low-power, dual-frequency, space-based GPS receiver becomes evident. As a software-defined receiver, FOTON has great potential for meeting this need.

Low Earth orbit single-frequency simulations show that 0.5 m precision orbit determination is attainable by FOTON, with potential for better performance using a Kalman filter. Dual-frequency LEO simulations yield 1.5 m precision in the presence of ionospheric delays; this could also be improved by implementing a Kalman filter that processes raw dual-frequency measurements rather than ionosphere-corrected single-frequency measurements.

With a time to first fix of approximately 45 seconds, FOTON could be duty-cycled to conserve power. For example, operating a total of 8 hours per day, it would consume 1.5 W orbit average power instead of 4.5 W. FOTON could operate less frequently if needed by relying on a high-fidelity Kalman filter to make up for the fewer measurements. Because FOTON is a software-defined receiver, such settings could be changed on-orbit.

Another advantage of FOTON's versatility as a software-defined receiver is that, with slight modifications to its configuration file and using an external OCXO as a timing reference, FOTON can navigate in geosynchronous

orbits. Tracking signals from the GPS transmitting antenna main lobe, FOTON is able to navigate within 10 m horizontal and 200 m vertical precision. With some additional modifications, such as data bit wipe-off and long coherent accumulation, FOTON should also be able to track signals from the first side lobe. This would allow FOTON to track more than four SVs, further increasing navigation precision.

In addition to FOTON's potential for precise orbit determination in LEO and GEO, it could also be developed into a radio occultation sensor. Capable of tracking signals down to the surface of the Earth, FOTON could be modified to map tropospheric as well as ionospheric profiles during occultations. This would allow such missions as COSMIC to be performed at a fraction of the cost.

# Appendix

# Appendix 1

# Complete LEO Benchmark Test Results

Presented here are the complete results of the LEO single-frequency benchmark testing discussed in Chapter 3. Table 1.1 shows the raw observable RMS errors for each of the six test cases, along with the corresponding test results of four other receivers tested by Holt [9]. The table is followed by plots of the observable double-differences for each test case. The first plot in each group was generated without the time-tag correction, the second plot after the correction. Test 3 shows no data because the simulator log file did not record any data for one of the SVs needed in this test.

Table 1.1: LEO Benchmark Testing Observables Noise

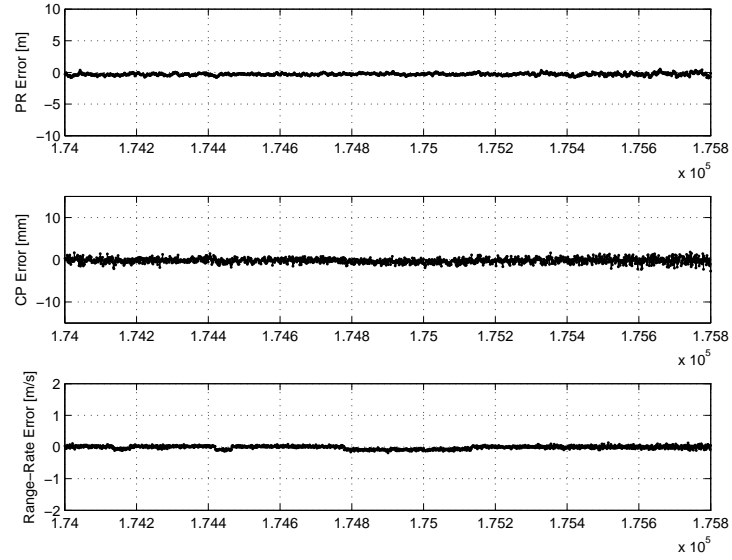| Test | Observable | FOTON | Architect | Orion | BlackJack | NovAtel |
|---|---|---|---|---|---|---|
| 1 | PR [m] | 0.1455 | 0.9258 | 0.9477 | 0.1553 | 0.0991 |
| | Phase [mm] | 0.5286 | 0.9323 | 0.9253 | 0.5030 | 1.1970 |
| | PR Rate [m/s] | 0.0503 | 0.1407 | 0.1414 | 0.0010 | 0.0745 |
| 2 | PR [m] | 0.1449 | 0.9037 | 0.9193 | 0.1025 | 0.1121 |
| | Phase [mm] | 0.5734 | 0.9227 | 1.0890 | 0.4270 | 1.2567 |
| | PR Rate [m/s] | 0.0537 | 0.1382 | 0.1440 | 0.0010 | 0.0359 |
| 3 | PR [m] | N/A | 0.9015 | 0.9559 | 0.1323 | 0.1226 |
| | Phase [mm] | N/A | 1.0899 | 1.0699 | 0.4105 | 1.3715 |
| | PR Rate [m/s] | N/A | 0.1419 | 0.1561 | 0.0010 | 0.0351 |
| 4 | PR [m] | 0.1548 | 0.9131 | 0.9029 | 0.1539 | 0.1267 |
| | Phase [mm] | 0.6805 | 1.1566 | 1.6478 | 0.9524 | 1.3559 |
| | PR Rate [m/s] | 0.0649 | 0.1526 | 0.1512 | 0.0010 | 0.0426 |
| 5 | PR [m] | 0.1708 | 0.8986 | 0.8960 | 0.1606 | 0.1217 |
| | Phase [mm] | 0.5784 | 1.1864 | 1.7767 | 0.6380 | 1.3480 |
| | PR Rate [m/s] | 0.0552 | 0.1469 | 0.1473 | 0.0010 | 0.0565 |
| 6 | PR [m] | 0.1920 | 0.9297 | 0.8942 | 0.1242 | 0.1285 |
| | Phase [mm] | 0.6255 | 1.2112 | 1.5659 | 0.2833 | 1.4228 |
| | PR Rate [m/s] | 0.0605 | 0.1466 | 0.1534 | 0.0010 | 0.0401 |
| Average | PR [m] | 0.1616 | 0.9121 | 0.9193 | 0.1381 | 0.1185 |
| | Phase [mm] | 0.5973 | 1.0832 | 1.3458 | 0.5357 | 1.3253 |
| | PR Rate [m/s] | 0.0569 | 0.1445 | 0.1489 | 0.0010 | 0.0475 |

Figure 1.1: SV 2-28 Double Difference, No Time Tag Fix-up
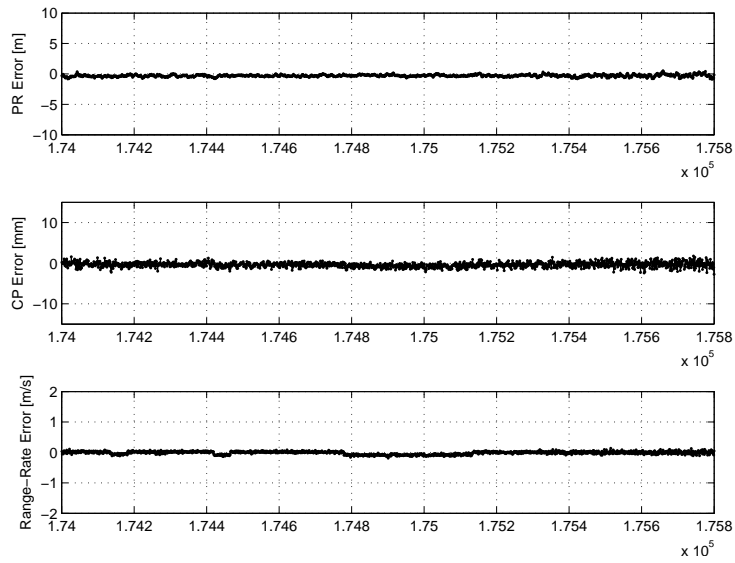


Figure 1.2: SV 2-28 Double Difference, Time Tag Fix-up
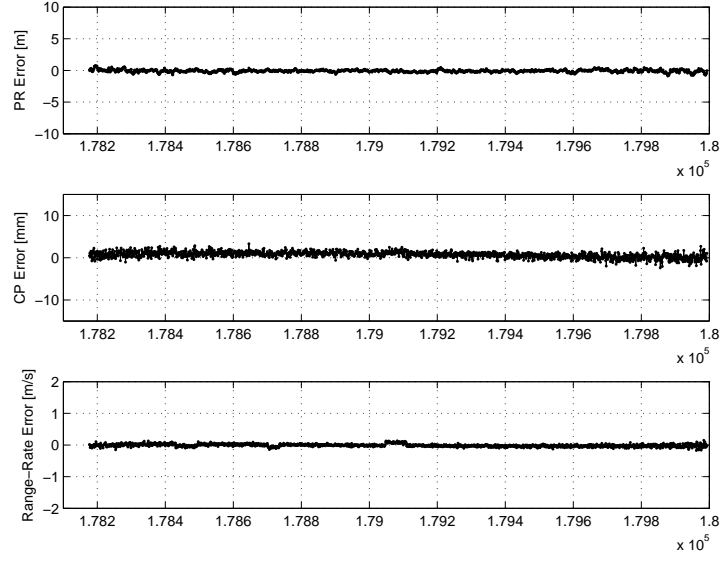
79

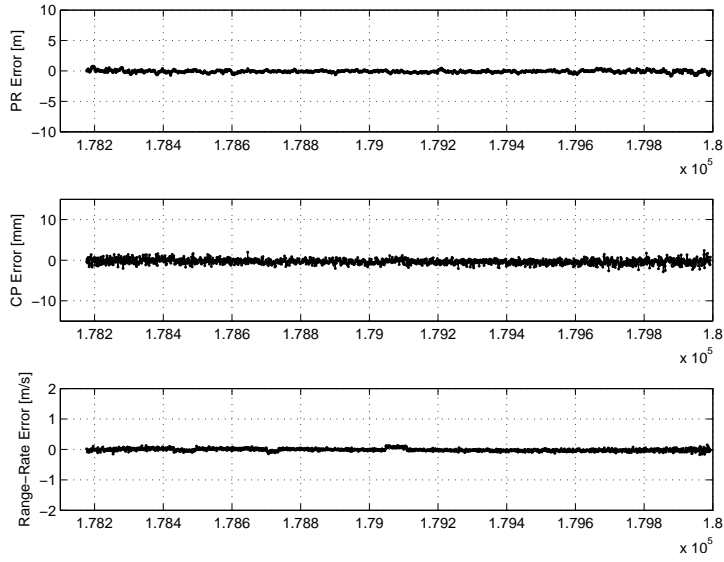Figure 1.3: SV 14-29 Double Difference, No Time Tag Fix-up



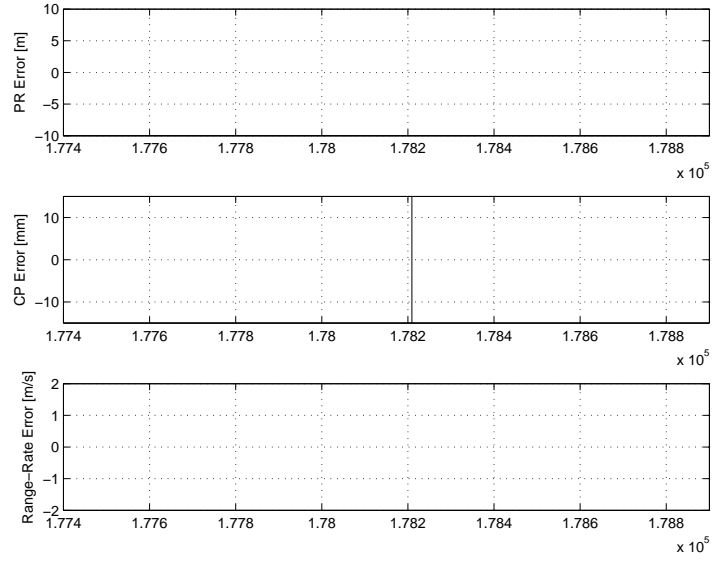Figure 1.4: SV 14-29 Double Difference, Time Tag Fix-up

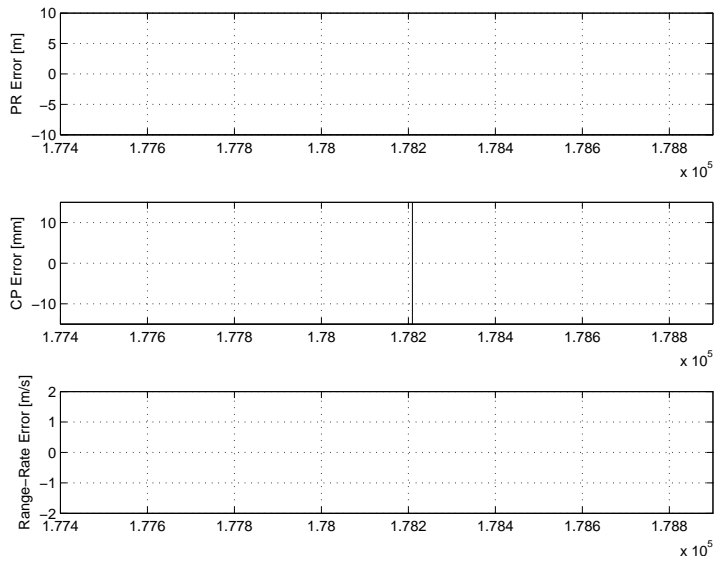Figure 1.5: SV 3-15 Double Difference, No Time Tag Fix-up


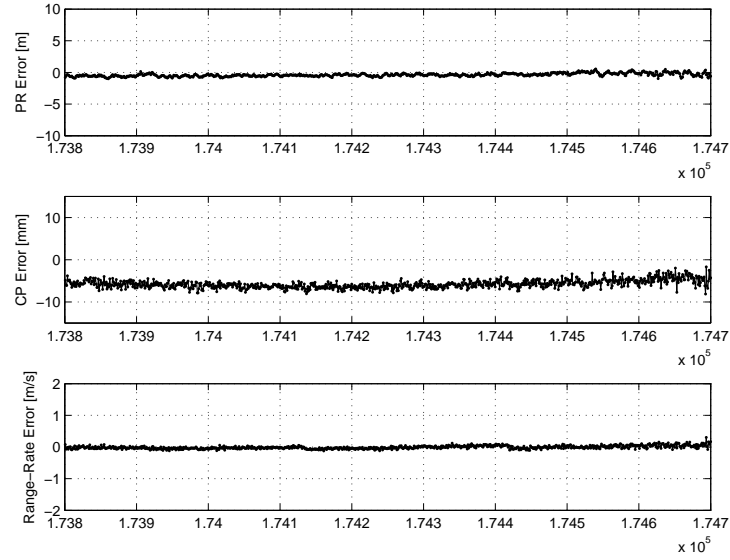
Figure 1.6: SV 3-15 Double Difference, Time Tag Fix-up

81
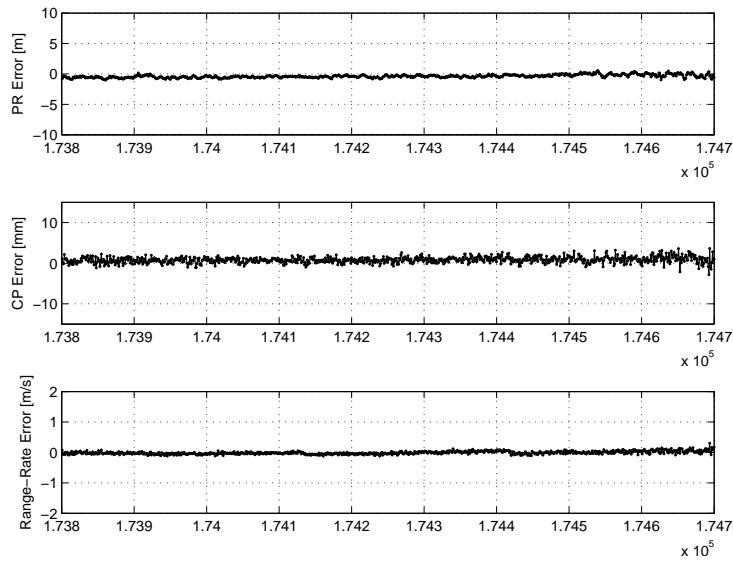
Figure 1.7: SV 21-28 Double Difference, No Time Tag Fix-up



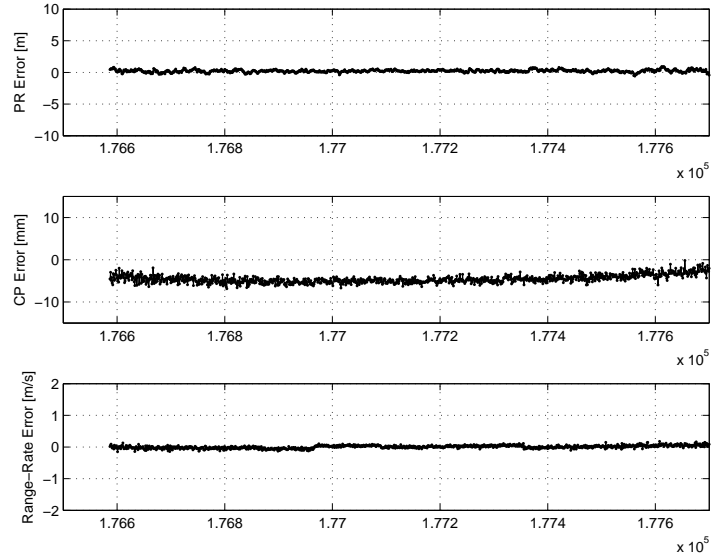Figure 1.8: SV 21-28 Double Difference, Time Tag Fix-up

82

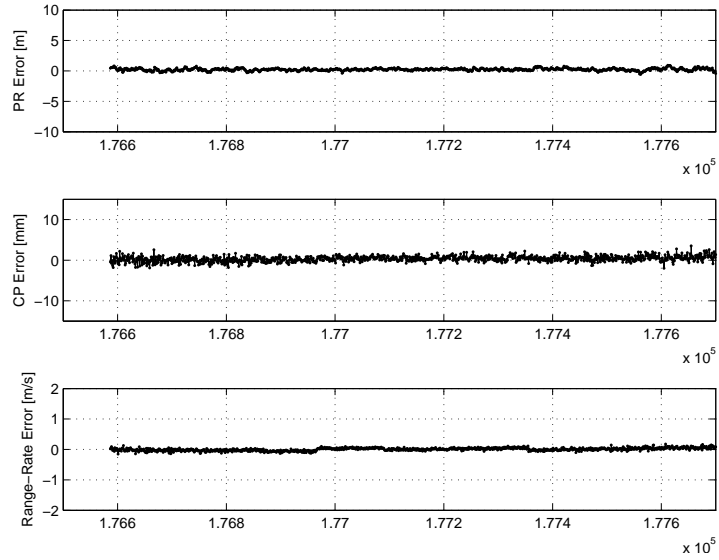Figure 1.9: SV 13-22 Double Difference, No Time Tag Fix-up



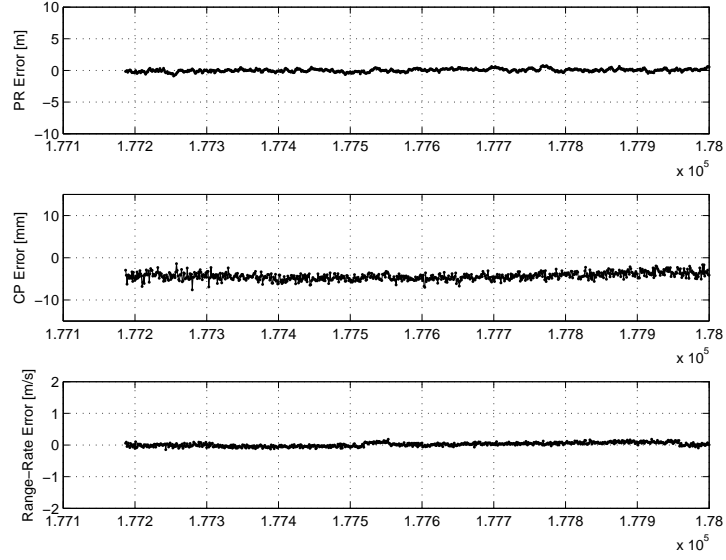Figure 1.10: SV 13-22 Double Difference, Time Tag Fix-up

83

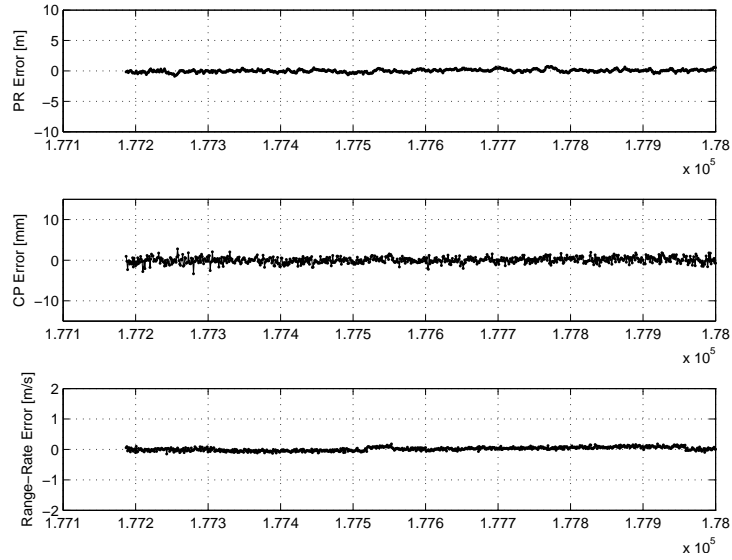Figure 1.11: SV 6-17 Double Difference, No Time Tag Fix-up



Figure 1.12: SV 6-17 Double Difference, Time Tag Fix-up

84

# Bibliography

[1] FOTON Sensor Preliminary Specifications. Technical report, The University of Texas at Austin, 2010.

[2] D. Bobyn. L1/L2 GPS Receiver Front End Hardware Technical Description. Technical report, Cornell University, 2010.

[3] *http://www.cosmic.ucar.edu/*. Accessed November 21, 2011.

[4] Francis Czopek and Scott Shollenberger. Description and Performance of the GPS Block I and II L-Band Antenna and Link Budget. *1993 Institute of Navigation Conference*, 1993.

[5] *http://fastrac.ae.utexas.edu*. Accessed November 21, 2011.

[6] *http://www.gpsworld.com*. Accessed November 16, 2011.

[7] *http://www.csr.utexas.edu/grace/*. Accessed November 21, 2011.

[8] G. Holt. Benchmark Testing for Spaceborne Global Positioning System Receivers. Master's thesis, The University of Texas at Austin, May 2002.

[9] G. Holt, E. G. Lightsey, and O. Montenbruck. Benchmark Testing for Spaceborne Global Positioning System Receivers. *2003 AIAA GNC Conference*, August 2003.

[10] T. Humphreys, M. Psiaki, and P. Kintner. GNSS Receiver Implementation on a DSP: Status, Challenges, and Prospects. *2006 ION GNSS Conference*, September 2006.

[11] P. Misra and P. Enge. *Global Positioning System - Signals, Measurements, and Performance.* Ganga-Jamuna Press, Lincoln, MA, 2nd edition, 2006.

[12] *http://spaceflight.nasa.gov/realdata.* Accessed March 1, 2011.

[13] B. O'Hanlon, M. Psiaki, P. Kintner, and T. Humphreys. Development and Field Testing of a DSP-Based Dual-Frequency Software GPS Receiver. *2009 ION GNSS Conference*, 2009.

[14] B. O'Hanlon, M. Psiaki, S. Powell, J. Bhatti, T. Humphreys, G. Crowley, and G. Bust. CASES: A Smart, Compact GPS Software Receiver for Space Weather Monitoring. *2011 ION GNSS Conference*, 2011.

[15] M. Psiaki. Satellite Orbit Determination Using a Single-Channel Global Positioning System Receiver. *Journal of Guidance, Control, and Dynamics*, 25(1):137–144, 2002.

[16] *http://radionavlab.ae.utexas.edu.* Accessed November 21, 2011.

[17] Byron Tapley, Bob Schutz, and George Born. *Statistical Orbit Determination.* Elsevier Academic Press, 2004.